JGR Solid Earth

RESEARCH ARTICLE
10.1029/2018JB017074

Subsurface Characterization of the Pennsylvanian Clare Basin, Western Ireland, by Means of Joint Interpretation of Electromagnetic Geophysical Data and Well-Log Data

Joan Campanyà[1,2,3], Xènia Ogaya[1], Alan G. Jones[1,4], Volker Rath[1], Brian McConnell[5], Peter D.W. Haughton[6], Juanjo Ledo[7], Colin Hogg[1], Sarah Blake[1,6], and Andrea Licciardi[1,8]

[1]School of Cosmic Physics, Geophysics Section, Dublin Institute for Advanced Studies, Dublin, Ireland, [2]Now at School of Physics, Trinity College Dublin, Dublin, Ireland, [3]School of Cosmic Physics, Astronomy and Astrophysics, Dublin Institute for Advanced Studies, Dublin, Ireland, [4]Now at Complete MT Solutions Inc., Ottawa, Canada, [5]Geological Survey of Ireland (GSI), Dublin, Ireland, [6]Irish Centre for Research in Applied Geosciences, University College Dublin, Dublin, Ireland, [7]GEOMODELS Research Institute, Departament de Dinàmica de la Terra i l'Oceà, Facultat de Geologia, Universitat de Barcelona, Barcelona, Spain, [8]Géosciences Rennes, University of Rennes 1, Rennes, France

Key Points:
- A new method for integrating passive electromagnetic geophysical data and well-log data for basin characterization and interpretation is reported
- Variations in shale character in the subsurface were mapped, with potential applications in basins elsewhere
- The hypothesis of fluid advective heating to explain the high maturity levels of the organic material is supported

Supporting Information:
- Supporting Information S1

Correspondence to:
J. Campanyà,
joan.campanya@cp.dias.ie

Citation:
Campanyà, J., Ogaya, X., Jones, A. G., Rath, V., McConnell, B., Haughton, P. D. W., et al (2019). Subsurface characterization of the Pennsylvanian Clare Basin, western Ireland, by means of joint interpretation of electromagnetic geophysical data and well-log data. *Journal of Geophysical Research: Solid Earth*, *124*, 6200–6222. https://doi.org/10.1029/2018JB017074

Received 26 NOV 2018
Accepted 24 MAY 2019
Accepted article online 4 JUN 2019
Published online 9 JUL 2019

Abstract The integration of passive electromagnetic geophysical data and well-log data for basin characterization and interpretation has been investigated in the Clare Basin, western Ireland. The Clare Basin is overmature and has a clear contrast in electrical resistivity between the Clare Shale Formation, a widespread organic rich shale unit, and the surrounding stratigraphy. The electrical resistivity distribution beneath the Clare Basin was determined by means of three-dimensional (3-D) joint inversion of three distinct and differently sensitive electromagnetic parameters: (1) the MT impedance tensor (Z), (2) the geomagnetic transfer function (T), and (3) the interstation horizontal magnetic transfer function (H). Well-log data from a local exploration well, Doonbeg-1, were analyzed by means of multivariate statistical methods identifying three groups with distinct resistivity values. The groups were propagated along the basin using the 3-D electrical resistivity model, showing those regions in the basin with significant organic content at high maturity stage. The lack of continuity of these regions supports the hypothesis of advective fluid heating as the cause of the high maturity levels. The results also help to define the geometry of the basin at depth and have identified an area within the basin, near the Loop Head, where organic-rich clay/shale is either poorly developed, and/or the organic matter is less mature and less conductive. Finally, the potential of the basin for both CO_2 storage and geothermal energy was considered, supporting the use of the Clare Basin as a potential site for geothermal energy but not for the storage of CO_2.

1. Introduction

The integration of geophysical data and well-log data for the understanding and interpretation of the subsurface geology and the related physical properties has been investigated in Ireland as part of the IRECCSEM project (Irish Carbon Capture, Sequestration and Storage study using EM methods), funded by Science Foundation Ireland. The aim of the project is to evaluate and further develop electromagnetic geophysical imaging methods, which are desirable for the safe and effective use of subsurface resources, for uses such as long-term carbon storage as well as the development of geothermal energy.

An area of West Clare, Ireland (Figure 1), was the focus of the study that involved using a multidisciplinary approach integrating electromagnetic (EM) passive geophysical data and well-log data, including electrical resistivity, sonic velocity, neutron porosity, and gamma ray logs. The area is underlain by part of the Clare Basin (also known as the Shannon Basin and Western Ireland Namurian Basin) that contains a succession of Mississippian limestones (>2-km thick) overlain by a largely Pennsylvanian clastic succession over 2.2-km thick. The transition from limestones to the clastic succession is characterized by shales (Clare Shale Formation) that in places are >200-m thick and that contain abundant organic matter with high levels of thermal maturation (R_o 5–6) and pyrite. The presence of abundant organic matter with high thermal maturation levels and pyrite decrease the electrical resistivity values of the shales, being significantly lower than the surrounding sedimentary rocks. The presence of such a strong contrast in resistivity makes EM geophysical methods ideal for (1) imaging the distribution of the shales in the subsurface and (2) hence to better

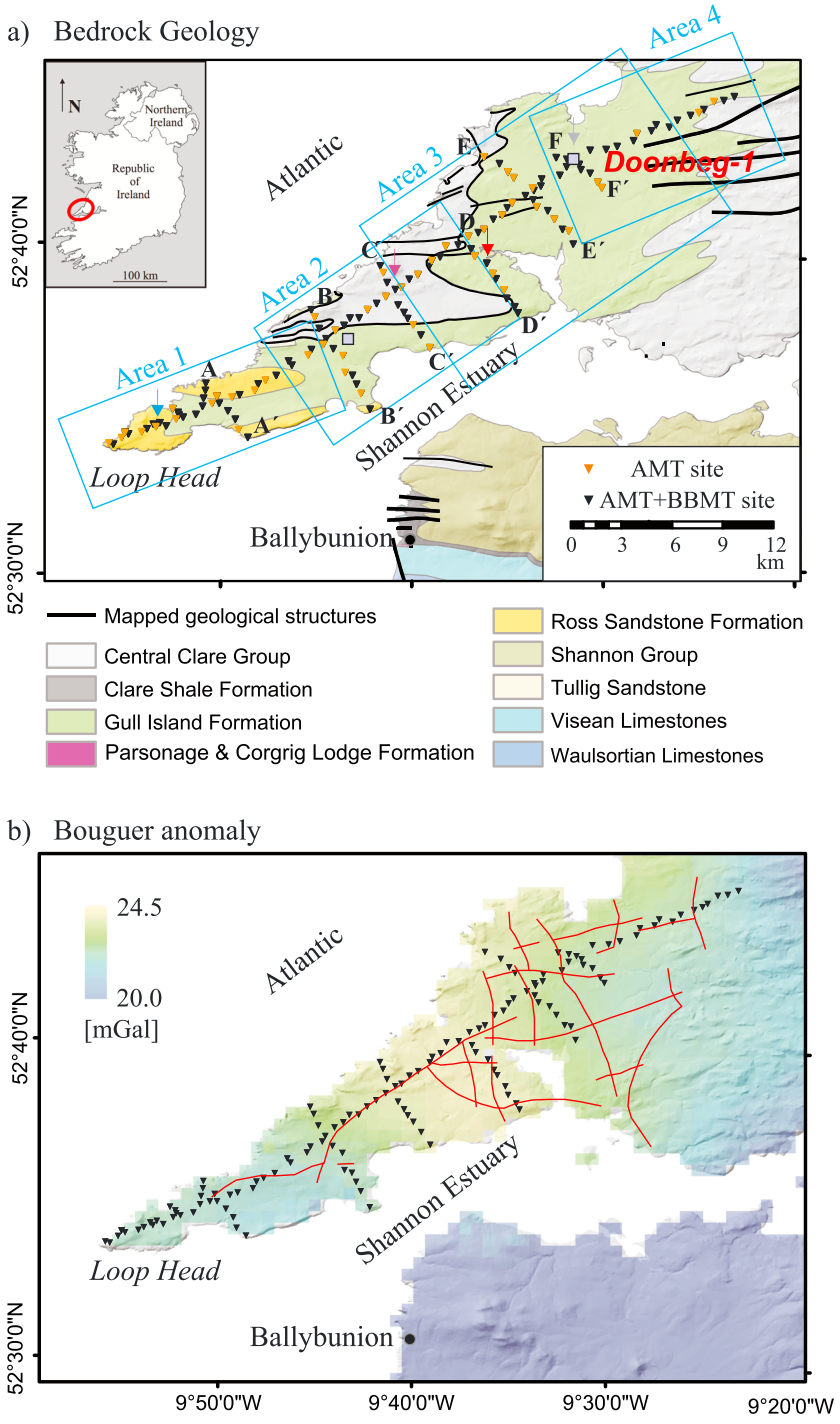

Figure 1. (a) Geological and (b) Bouguer anomaly maps with the location of the EM geophysical sites (inverted triangles), and the location of Doonbeg-1 Well (red). Blue rectangles define the segments of interest of the MT models, where the grid is refined. AA′-FF′ are the cross profiles crossing the main axial profile. Purple squares show the sites used for remote reference for BBMT data. Color arrows indicate the sites used as neighboring sites for H responses. Red lines in Figure 1b indicate the locations where seismic data was acquired (Farrelly et al., 2008). Geological Map was provided by Geological Survey Ireland. Gravity data was provided by Dublin Institute for Advanced Studies. AMT = audio-magnetotelluric; BBMT = broadband magnetotelluric.

constrain the geometry of the basin, possible trends in shale development and composition, and the processes leading to the high maturation levels.

EM geophysical methods are broadly used to image the electrical resistivity distribution of the subsurface at several depths of penetration, from a few tens of meters to hundreds of kilometers, and for different academic or commercial purposes (Berdichevski & Dmitriev, 2008; Chave et al., 2012). With dense station coverage, EM passive geophysical methods can unravel shallow structures providing valuable information, particularly when integrated with additional data sets (Blake et al., 2016; Falgàs et al., 2011; Gabàs et al., 2016; García-Yeguas et al., 2017; Ogaya et al., 2016). An old exploration well (Doonbeg-1; Figure 1a) in the Clare Basin, dating from 1962, provides important constraints on the main lithologies and the petrophysical properties (including electrical resistivity) of the rocks in the northwestern part of the study area.

This paper presents the results of integrating the Doonbeg-1 well data (which provides local and detailed information), with a new 3-D electrical resistivity model for the West Clare area (which provides regional and "fuzzy," i.e., less well resolved information). The Doonbeg-1 well data were analyzed using multivariate statistical methods defining rock intervals with similar physical properties. The new electrical resistivity model results from the 3-D joint inversion of three different types of passive EM responses. The measurement array was divided into four areas with at least three MT sites overlapping with the neighbor areas (blue rectangles in Figure 1a) in order to compute a higher resolution geoelectrical model within a reasonable time and at lower computational costs. Joint interpretation of the well-log data and the electrical resistivity model provided a new subsurface model for the basin and the organic-rich shales it contains. Comparison with additional geophysical data including seismic reflection and gravity data helped constrain the interpretation of the presented results and evaluate the potential use of the basin for both CO_2 storage and geothermal energy.

2. Geological Setting

2.1. Tectonic Context

The Clare Basin is one of a number of Carboniferous basins that developed in northwestern Europe as a consequence of a phase of Mississippian extension (358.9–323.2 Ma). The basin is underlain by an important crustal suture zone, the Iapetus Suture, that formed during the Caledonian orogenic cycle (490–390 Ma) with the oblique closure of the Iapetus Ocean during the Silurian (Chew & Strachan, 2014). Following the collision, terrestrial sediments were deposited during the Devonian (e.g., Graham, 2009), with the onset of predominantly carbonate deposition as a result of a regional marine transgression during earliest Carboniferous (Tournaisian; McDermot & Sevastopulo, 1972). Several local depocenters, including the Clare Basin, developed across Ireland during the Tournaisian and Viséan (358.9–330.9 Ma) as a result of extensional tectonism and subsidence (e.g., de Morton et al., 2015; Somerville, 2008; Strogen et al., 1996). These basins were principally controlled by movement on NE-SW oriented structures, the orientation of which was inherited from underlying Caledonian trending features (Worthington & Walsh, 2011). Extensive carbonate deposition continued in Ireland until a switch to terrigenous mud and sand deposition at the end of the Viséan Stage (Sevastopulo & Wyse Jackson, 2009).

The axis of the Clare Basin coincides with the Iapetus Suture Zone in the area of the Shannon Estuary (Pyles, 2008). Broad regional subsidence of the Clare Basin started early in the regional crustal stretching during the Lower Carboniferous with an acceleration in subsidence rates along the axis of the Shannon Estuary accommodating a thick succession of initially shallow but then deepwater limestones. During the Serpukhovian Stage (330.9 to 323.2 Ma), there was a switch to anoxic black shale facies (Braithwaite, 1993; Hodson, 1953) reflecting the arrival of clastic input from the southwest into a basin axis that, at this time, was in deep water with a stratified water column. Subsequently, a sandy deep-sea fan system advanced into the basin from the SW. This was followed by a predominantly silty succession interpreted as slope deposits, and ultimately by delta systems arranged in cyclothems reflecting progradation and retreat of the shoreline driven by fluctuations in relative sea level. In the Late Carboniferous, the basin was inverted and structurally deformed by the Variscan Orogeny, producing open east-west trending folds, and variably developed foliation and fractures. Apart from a thin Quaternary overburden that masks much of the inland subcrop, no rocks younger than Carboniferous age are preserved.

2.2. Stratigraphy

The Carboniferous succession in the Shannon Estuary area can be divided into five main units, which from older to younger are Viséan Limestones, the Clare Shale Formation, the Ross Sandstone Formation, the Gull Island Formation, and the Central Clare Group. These are now briefly described highlighting features that will impact on electrical properties (see Best & Wignall, 2016; Farrelly et al., 2008, for a more detailed account).

2.2.1. Viséan Limestones

The Viséan Limestones comprise a range of carbonate rock types including a thick (>800 m) Waulsortian succession of micritic mud mounds (largely Tournasian) overlain by remobilized carbonate and, in the Late Viséan, by calciturbidites. The top of the Viséan Limestone has a maximum depth of 1,300 m to the southwest of the Doonbeg-1 well (Somerville & Strogen, 1992).

2.2.2. Clare Shale Formation

The Clare Shale Formation is composed of dark grey shale interbedded with thin horizons of laminated, organic-rich shale, commonly with large carbonate concretions (Braithwaite, 1993), and chert levels. The Clare Shale Formation records tranquil, anoxic to dysoxic deposition over the entire Clare Basin during the early Namurian. The pyrite content of the sediments is high (Braithwaite, 1993). A maximum known thickness of 275 m is encountered in the Doonbeg-1 well, where the top of the Clare Shale Fm is at ~800-m depth. Although there are no outcrops of Clare Shale in west Clare, it is well exposed south of the Shannon at Ballybunion (see location on Figure 1a) and in the inner Shannon estuary.

2.2.3. Ross Sandstone Formation

The Ross Sandstone Formation outcrops along the coast surrounding the Loop Head Peninsula (see Figure 1a) and is also known from "behind-outcrop" boreholes in the area (Pierce et al., 2018). This formation consists of bedded sandstones (approximately 65%) together with subordinate interbedded shales, a number of thin (dcm to meter scale) condensed sections (black, fossiliferous, and locally pyritized shales) and slumped silty units. It is up to 495-m thick in the Loop Head area (Pierce et al., 2018) and a similar thickness is present at Ballybunion. The age-equivalent section in North Clare is in shale facies and very much thinner (only a few meters), demonstrating that the sandy succession was confined to the deeper basin axis where it comprises a number of stacked, relatively small (10s km radius), sand-rich submarine fan systems.

2.2.4. Gull Island Formation

The Gull Island Formation (Figure 1a) is mud dominated with siltstone and some fine sandstone, with sandstone content decreasing upward. It is characterized by numerous slumped intervals with minor channels and lobes (Martinsen, 1989; Pyles, 2008). The upper part of the Gull Island Formation consists of a mudstone-dominated succession that coarsens slightly upward to siltstone with some sandstone filled turbidite channels. The Gull Island Formation is thickest in the axial region near the Shannon Estuary and the southwest County Clare coast, reaching thicknesses of 550 m (Martinsen et al., 2003).

2.2.5. Central Clare Group

The delta systems of the Central Clare Group transitionally overlie the Gull Island Formation and comprise repeating successions or cyclothems of shallowing upward prodelta, delta front, and delta top deposits separated by condensed fossiliferous mudstone "marine bands" (Rider, 1974; Sevastopulo & Wyse Jackson, 2009). This group has a known minimum thickness of 900 m, and we do not see the top of the succession.

3. Previous Geophysical Studies

3.1. Well-Log Data (Doonbeg-1 Well)

The Doonbeg-1 well was drilled in the 1960s and reached a depth of 3,200 m (Information Handling Services (IHS), 2008). A suite of petrophysical logs as well as total organic carbon (TOC) and the vitrinite reflectance (Ro) coefficients of the organic content were recorded. In this study, four petrophysical logs were used to characterize the subsurface geology: the electrical resistivity, sonic velocity, neutron porosity, and gamma ray logs. In addition, Ro data contributed to constrain the thermal evolution of the basin. The same formations as described before in the stratigraphy section were drilled, although the top and thickness of each formation may slightly differ from the values presented above. Figure 2 shows the well-log data of the presented physical properties and the depths of the main formations.

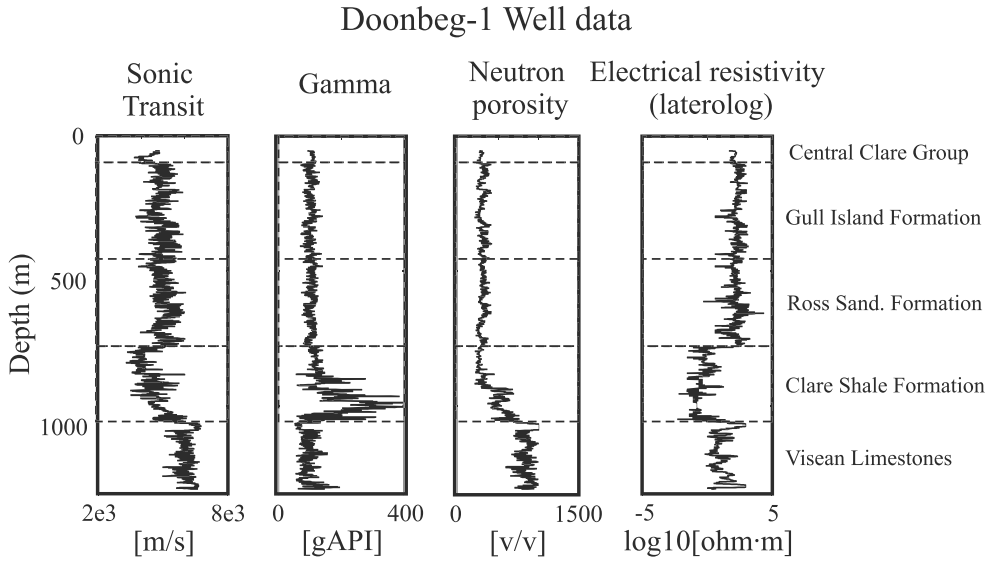

Figure 2. Data from Doonbeg-1 well up to 1,250-m depth including Sonic velocity, Gamma ray, Neutron porosity, and Electrical resistivity data. Horizontal dashed lines define the main lithological units.

3.1.1. Petrophysical Data Sets

The electrical resistivity profile shows relatively high electrical resistivity values (between 50 and 1,000 Ωm) at shallower depths (from 0- to 785-m depth), with alternated sharp and thin decreases in resistivity (<10 Ωm) caused by the presence of thin layers of clay or shale (possibly condensed sections in the Ross Sandstone Formation). At approximately 785-m depth, at the level of the Clare Shale Formation, the electrical resistivity profile has a dramatic decrease in resistivity dropping to electrical resistivity values smaller than 1 Ωm. The electrical resistivity values rise again at around 1,060-m depth, at the top of the Viséan Limestones, to values between 1 and 1,000 Ωm. The large range of variation in resistivity within the upper part of the Viséan Limestones is interpreted to reflect the presence of relatively thin layers of clay/shale (conductive) within the limestone (resistive). A similar feature is seen at outcrop at Ballybunion and is consistent with the presence of deep-water limestones (calciturbidites) in the Doonbeg area. The sonic velocity profile shows average values between 4,000 and 5,000 m/s for the top formations until a significant decrease is observed when reaching the top of the Clare Shale Fm (<4,000 m/s). Then velocity rises again with depth until it reaches the Viséan limestones, with sonic velocity values between 5,000 and 6,000 m/s. Relatively low and constant neutron porosity values are observed above the top of the Clare Shale Fm (200 to 400 American Petroleum Institute (API) units. It is not until we get within the Clare Shale Formation that there is a significant increase in the compactness of the sediments, reaching even higher neutron porosity values within the Viséan Limestones (500 to 1,000 API). Gamma ray values for the top formations are relatively low (between 70 and 100 gAPI), but the basal part of the Clare Shale Formation has higher values (between 100 and 400 API gamma ray unit (gAPI)). Gamma ray values decrease again within the limestones to values less than 100 gAPI, although a few local increases are observed associated with the inferred presence of clay/shale.

3.1.2. Organic Matter and Thermal Evolution

Organic matter is abundant in most of the shale sequences, especially in the interval between 790 and 1,060 m, within the Clare Shale Formation, with total organic carbon values of up to 15%. Vitrinite reflectance (Ro) data show the entire drilled section is very high in rank, and most of the samples analyzed fall in the meta-anthracite maturity zone (Ro greater than 4.0%) suggesting that the Clare Shale Formation is overmature. Interestingly, data from the Doonbeg-1 well do not show the normal increase in maturation with depth but rather a more complex profile with an apparent reverse gradient in the upper part of the Viséan Limestones near the base of the Clare Shale Formation. Simple burial seems inadequate to explain these data, and fluid advective heating has been suggested as the most likely mechanism (Fitzgerald et al., 1994; Goodhue & Clayton, 1999).

3.1.3. The 2-D Seismic Reflection Data

The earliest large-scale geophysical survey in west Clare was a 2-D reflection seismic program executed in 1962 by Ambassador Oil, which comprised 27 lines with a total length of approximately 150 km. This data set was reinterpreted by Farrelly et al. (2008) that highlighted a significant impedance contrast associated with the top of the Viséan Limestones. Although less certain, but consistent with the available geological and geophysical constraints, the seismic data were also used to estimate the depth to the top of the Clare Shale and the Ross Sandstone formations. These data reveal that currently the thickest preserved succession of Namurian clastic rocks is located just to the SW of Doonbeg-1 well, with a significant shallowing to the southwest on the Loop Head Peninsula where the Viséan Limestones rise from 1,200-m depth to around 800 m. It is in this region that the Ross Sandstone Formation reaches the surface. The Clare Shale Formation and the Viséan Limestones do not outcrop on the Loop Head Peninsula, but they are encountered in boreholes here (Pierce et al., 2018).

3.2. Gravity Data

The Clare Basin is dominated by an extensive high amplitude Bouguer anomaly covering most of west Clare. Although the origin of this feature is not well constrained, it has in the past been related to deep Ordovician volcanic rocks located beneath the Lower Carboniferous carbonate succession (Farrelly et al., 2008). A local increase of the Bouguer anomaly to the SW of Doonbeg-1 well (Figure 1b; Doonbeg-1 well is marked with a grey arrow in Figure 1a) coincides with what is the thickest preserved part of the basin, and the gravity values tend to decrease away from this. Figure S1, supporting information, shows the sites where gravity data was acquired.

4. EM Soundings

Electromagnetic (EM) tensor relationships, which contain information about the electrical resistivity properties of the subsurface geology, were obtained by relating different components of the Earth's natural electric and magnetic fields variations with time. In this study, we focused on three different EM tensor relationships: (1) the MT impedance tensor (***Z***; Cantwell, 1960; Rokityanski, 1961), (2) the less commonly used geomagnetic transfer function (***T***; Parkinson, 1962; Weise, 1962), and (3) the very rarely used interstation horizontal magnetic transfer function (***H***; Berdichevsky, 1968; Egbert & Booker, 1989; Schmucker, 1970, Soyer & Brasse, 2001).

The MT impedance tensor (***Z***) describes the linear relationship between the measured horizontal components of the electric (E_x, E_y) and magnetic (H_x, H_y) fields and is commonly applied to characterize the electrical resistivity values of the subsurface geology. The geomagnetic transfer function (***T***) describes the linear relationship between the vertical component of the magnetic field (H_z) and the horizontal components of the magnetic field (H_x, H_y). Although this function is not sensitive to the absolute electrical resistivity values, it is very useful to identify lateral resistivity contrasts. Finally, the interstation horizontal magnetic transfer function (***H***) describes the linear relationship between the measured horizontal magnetic field at one site (H_x^1,H_y^1,) and the horizontal magnetic field measured at a different site (H_x^2, H_y^2). This type of data, which is also not sensitive to the absolute electrical resistivity values of the subsurface geology, also helps define horizontal changes in resistivity. The main advantage of ***H*** is that it improves the consistency of the model as a whole, as the data between different stations, independently on the distance between them, are directly related. For a more detailed description of the advantages of complementing ***Z*** with ***T*** and ***H*** responses see (Campanya et al., 2016).

4.1. Data Acquisition

Data from a total of 140 MT sites were acquired in west Clare during summer of 2014 using audio-magnetotelluric (AMT) and broadband magnetotelluric (BBMT) Phoenix Geophysics MTU-V5 and –V8 systems (Figure 1). Horizontal electric and magnetic fields and the vertical magnetic field data were measured at each site. AMT data were recorded at all sites with an average distance between sites of 600 m. BBMT data were recorded at 87 of these sites, having an average distance between BBMT sites of 1,000 m. The AMT and BBMT sites were located along a main axial profile 46-km long and along six short cross profiles perpendicular to it (Figure 1a; AA′ to FF′ profiles). The AMT data were recorded overnight at the sites without BBMT

data. At the sites with BBMT data, AMT data were recorded for three hours during the daytime, and BBMT stations were left in the ground recording for at least two nights.

4.2. Data Processing

Electric and magnetic field time series were processed to obtain ***Z***, ***T***, and ***H*** response estimates using several processing algorithms (Egbert & Booker, 1986; Chave & Thomson, 2004; Smirnov, 2003) and software from Phoenix Geophysics (cascade code based on Wight & Bostick, 1980 with Least Trimmed Squares robust implementation of Jones & Jödicke, 1984). Due to the presence of anthropogenic noise, mostly from electric fences, two BBMT sites (Figure 1a, purple squares, one at the intersection of B-B′ with Axial profile and the other at the intersection of F-F′ with Axial profile), were constantly recording during the acquisition period, enabling the use of the remote reference (RR) method (Gamble et al., 1979; Gamble, 1979) and ELICIT (Campanyà et al., 2014) to improve the quality of the processing results. For the AMT data, RR was performed between stations measuring simultaneously at different locations. The RR method was applied to reduce the influence of correlated and uncorrelated local noise, as it can reduce bias and source effects of correlated noise. However, one of the main issues associated with RR is that the performance decreases for longer periods due to the reduced number of samples used when processing the MT data. The ELICIT method, based on interstation tensor relationships between electric and magnetic fields measured at different locations, was applied to increase the number of samples and improve the statistics when processing the data.

Sites at which most of the recording periods were dominated by noise were discarded. Sites with good quality data were cleaned removing the time intervals that were significantly affected by noise. Note that in these cases the data were deleted for all the components of the tensor relationship. Finally, we used periods between 0.0001 to 1,000 s (10,000 to 0.001 Hz) for ***Z*** data and between 0.01 and 1,000 s (100 to 0.001 Hz) for ***T*** and ***H*** data. ***H*** data, for which it is recommended that at least one reference site is recorded for the complete survey in order to have a common neighboring site for all the sites acquired, were only calculated for BBMT sites.

An error floor was added to the data sets to deal with deficiencies in the statistical data processing procedures, balance fit across the period range, and allow for systematic biases and limitations of the numerical models (not accounted in the statistical data errors). The error floor was selected with the aim of (1) having a relatively small total nRMS (i.e., <2), (2) having similar nRMS for all of the inverted data sets, and (3) avoiding a dominant group of periods and sites with normalized root mean squared (nRMS) values close to zero. If the selected error floors are too small the total nRMS will be large, but if the error floors are too large there will be a significant number of periods with nRMS values close to zero. Similar nRMS for all data sets suggest that the inverted data sets had a similar weight during the inversion process.

An error floor of 5% was imposed for all ***Z*** components, using 5% of $|Z_{xy}|$ for the Z_{xy} and Z_{xx} data (as they share the same electric field, i.e., E_x) and 5% of$|Z_{yx}|$for the Z_{yx} and Z_{yy} data (both share E_y) if the absolute value of the diagonal component was smaller than the absolute value of the off-diagonal component, respectively. This error floor attribution assumes that the error is primarily in the electric fields, so that the absolute error in E_x affects Z_{xx} and Z_{xy} equally, and similar for E_y and Z_{yx} and Z_{yy}. An absolute error floor of 0.025 was assumed for ***T*** and ***H*** responses. These errors are consistent with the errors assumed in other publications with both real and synthetic data performing individual and/or joint inversion to model the electrical resistivity values of the subsurface geology (Campanyà et al., 2016, 2018; Egbert & Kelbert, 2012; Habibian et al., 2010; Soyer & Brasse, 2001; Tietze & Ritter, 2013). These errors were assumed for the rest of the study, including the dimensionality analysis and the inversion process.

The influence of galvanic effects in the ***Z*** response estimates was evaluated by superimposing the ***Z*** responses of the sites from each area (Figure 3). Galvanic effects can influence each site individually by adding a shift on the apparent resistivity curve in 1-D and 2-D situations and by modifying the shape of the apparent resistivity and phase in a more general situation (i.e., Jones, 2011; Ledo et al., 1998). We analyzed the sites in each of the areas defined in Figure 1a separately (Figures 3a–3d) and all the sites simultaneously (Figure 3e). The absence of sites with large differences with respect to the dominate trend suggests that no large galvanic effects were present. In addition to this evaluation, we can already predict significant differences between the four areas in Figure 1a. The apparent resistivity curves and phases in Area 3 seems to be strongly affected by a conductive anomaly at periods between 0.1 and 50 s. This effect is also observed

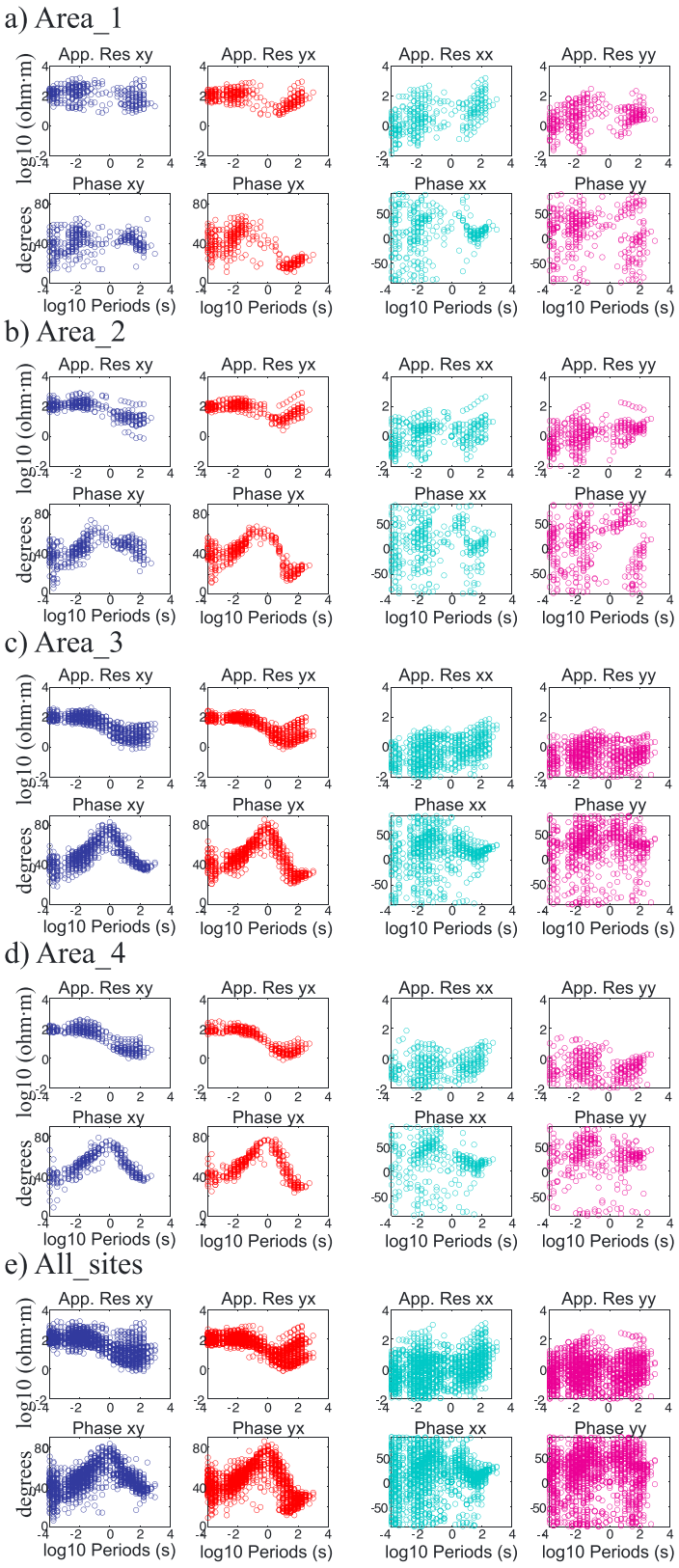

Figure 3. Apparent Resistivity and phase values for the *xy*, *yx*, *xx*, and *yy* components of the MT sites in the Loop Head Peninsula. (a) Sites from Area 1 in Figure 1a, (b) sites from Area 2 in Figure 1a, (c) sites from Area 3 in Figure 1a, (d) Sites from Area 4 in Figure 1a, and (e) all the sites.

Table 1
Inversion Parameters

	Area 1	Area 2	Area 3	Area 4
Data				
Num. Sites (AMT–BBMT)	32–18	31–15	54–33	25–17
Periods	0.0001 to 1,000 s	0.0001 to 1,000 s	0.0001 to 1,000 s	0.0001 to 1,000 s
Data Type	Phase 1: $\boldsymbol{Z}$ Phase 2: $\boldsymbol{Z}+\boldsymbol{T}+\boldsymbol{H}$	Phase 1: $\boldsymbol{Z}$ Phase 2: $\boldsymbol{Z}+\boldsymbol{T}+\boldsymbol{H}$	Phase 1: $\boldsymbol{Z}$ Phase 2: $\boldsymbol{Z}+\boldsymbol{T}+\boldsymbol{H}$	Phase 1: $\boldsymbol{Z}$ Phase 2: $\boldsymbol{Z}+\boldsymbol{T}+\boldsymbol{H}$
Mesh				
Num. Cells (x, y, z)	106 × 166 × 105	114 × 111 × 105	103 × 123 × 105	86 × 110 × 105
Central Mesh (x, y, z)	82 × 142 × 105	92 × 85 × 105	77 × 97 × 105	56 × 80 × 105
Size Horizontal Cells (m)	100 × 100	150 × 150	200 × 200	200 × 200
Increase Padding Cells	1.3	1.3	1.3	1.3
Vertical Size (m)	5	5	5	5
Topography/Bathymetry				
Increase Vertical Size	1.013	1.013	1.013	1.013
Inversion Parameters				
Resistivity of the Initial Model	Phase 1: 120 Ωm Phase 2: Average between 120 Ωm and results from Phase 1	Phase 1: 120 Ωm Phase 2: Average between 120 Ωm and results from Phase 1	Phase 1: 120 Ωm Phase 2: Average between 120 Ωm and results from Phase 1	Phase 1: 120 Ωm Phase 2: Average between 120 Ωm and results from Phase 1
Resistivity of the Ocean	0.3 Ωm (fixed)	0.3 Ωm (fixed)	0.3 Ωm (fixed)	0.3 Ωm (fixed)
Smoothing (x–y–z)	0.3–0.3–0.2	0.3–0.3–0.2	0.3–0.3–0.2	0.3–0.3–0.2
Ref. Model	Initial model	Initial model	Initial model	Initial model
Neighboring Site for $\boldsymbol{H}$ Responses	Blue Arrow Fig. 1a	Pink Arrow Fig. 1a	Red Arrow Fig. 1a	Gray Arrow Fig. 1a

Note. AMT = audio-magnetotelluric; BBMT = broadband magnetotelluric.

in Areas 2 and 4, although less accentuated in Area 2. Area 1, which is probably strongly affected by the presence of the highly conducting ocean, suggests a more resistive and complex environment than the rest of the basin.

The presence of the Atlantic Ocean and the Shannon estuary close to the area of study already indicates a 3-D geoelectrical environment. The performed dimensionality analysis (Text S2 in the supporting information) corroborates the need of a 3-D approach for modelling the subsurface beneath the area of study.

4.3. 3D resistivity Modelling

4.3.1. Inversion Process

Inversion processes were performed using the ModEM algorithm (Egbert & Kelbert, 2012; Kelbert et al., 2014) with the inclusion of $\boldsymbol{H}$ responses (e.g., Campanya et al., 2016). Each of the four areas in which the area of study was divided (Figure 1a, blue rectangles) was inverted separately. The main parameters assumed for the inversion process of the four areas are summarized in Table 1. The 3-D solution meshes were generated so as to include free cells between sites and ensuring that at the greatest depth of interest the vertical size of the cells were equal or smaller than the horizontal size of the cells. Due to the challenging coastal line to the west of the study area, the size of the cells was reduced in this region to account for the coastal effect. The topography and bathymetry were included in all the models using constant cell sizes and fixing the resistivity of the ocean at 0.3 Ωm.

Several tests were performed to choose the initial electrical resistivity model and the smoothing parameters. The starting model was chosen after inverting the $\boldsymbol{Z}$ responses, which are sensitive to lateral and vertical variations and to the absolute electrical resistivity values of the subsurface geology. Values between 20 and 500 Ωm were tested for the initial homogeneous half space model assuming smoothing values of 0.3 for the horizontal and vertical directions. Initial models with poor fit to the data after the inversion process were excluded. The electrical resistivity value of 120 Ωm for the homogeneous starting model was then chosen within the range of starting models that best fit the data of the four areas. In the case of the ModEM code, we also have to choose horizontal and vertical smoothing parameters. Additional tests were conducted to define the values for the smoothing parameters. Using 120 Ωm for the initial model, several

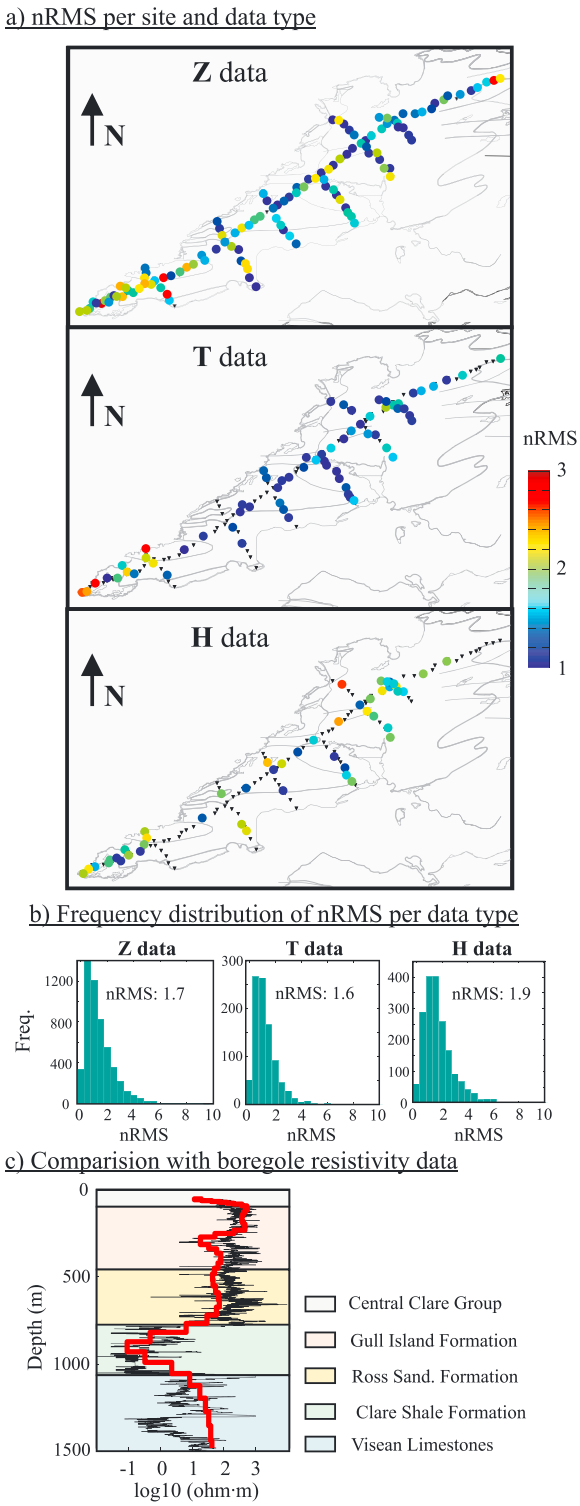

Figure 4. Fit of the data from the MT models, for each type of data. Black inverted triangles are sites with no data. (a) nRMS per site and data type (*Z*, *T*, and *H*), (b) nRMS per data type (*Z*, *T*, and *H*) in histogram format. The specified nRMS value in each subfigure is the average value per each type of data. (c) Comparison of the electrical resistivity values at depth below Doonbeg-1 between the MT model (red line) and the resistivity log data from Doonbeg-1 well (black line). Colored rectangles represent the main geological formations.

combinations of horizontal and vertical smoothing parameters were applied with values between 0.1 and 0.6 (always assuming the same smoothing values for north-south and east-west directions). Inversions with largest smoothing values that fit the data of the models for the four areas were chosen to define the smoothing values for the final inversions, with the aim of avoiding the presence of artefacts generated by the inversion process.

Once the main parameters were selected, the inversion process for each area was undertaken in two phases. During the first phase we inverted only the ***Z*** response estimates. The resulting model from the inversion was averaged, on a log10 scale, with the initial homogeneous model (half space model of 120 Ωm). The aim of the average was to obtain a new initial model in which the main geoelectrical structures were fuzzily defined, but in which, there were no strong contrasts in resistivity, thus facilitating to incorporate the information from ***T*** and ***H*** responses. During the second phase, the model resulting from phase 1 was taken as the initial model for the joint inversion of ***Z***, ***T***, and ***H*** response estimates. The fact that the initial model was based on the results from the ***Z*** inversion facilitated the convergence of ***Z***, ***T***, and ***H*** during the joint inversion. Due to the complexity of the geology at depth, the reference sites for the ***H*** data were selected after the inversion of the ***Z*** data, choosing regions with no major anomalies below the reference site, as recommended by Campanya et al. (2016).

Although no major galvanic effects were identified (Figure 3), as a 3-D modelling approach was used to recover the electrical resistivity values of the subsurface with a fine discretization in the uppermost part of the model, it was expected that the models were not significantly affected by near-surface galvanic distortion effects at the target depths (Farquharson et al., 2002; Meqbel et al., 2014). In addition, the inversion of ***T*** and ***H*** data, which are unaffected by galvanic distortion of the electric fields (Chave & Jones, 1997; Chave & Smith, 1994), would decrease the susceptibility of the resulting model to galvanic effects.

4.3.2. Fit of the Data

The fit of the data and the ability of the model to reproduce the subsurface electrical resistivity values were evaluated based on three different measures: (1) nRMS per site and data type; (2) frequency distribution of nRMS per data type, and (3) comparison between the electrical resistivity data from Doonbeg-1 well and the electrical resistivity values from the inversion process at this site. Figure 4a shows the nRMS per site and data type. All sites are fitted similarly independently of their location, except ***Z*** and ***T*** data for the sites at the far western end of the survey on the Loop Head Peninsula (Area 1). The numerical impediments for accurately modelling the coastal effects in Area 1 are probably the cause of the slightly larger nRMS values in this area. The fit of the data for each component of the used tensor relationships is presented in Figure S3 (supporting information). Figure 4b shows the frequency distribution of nRMS data type in histogram format, with mean nRMS values of 1.7 for ***Z***, 1.6 for ***T***, and 1.9 for ***H***. Although the mean nRMS for each of parameters is not identical, which ideally would be the case for the joint inversion, the difference in nRMS between ***Z***, ***T***, and ***H*** is smaller than 0.3, which suggests that an adequate error values were assumed for the joint inversion. No significant sequential groups of periods or groups of neighboring sites with nRMS values larger than 4 were observed for any type of data.

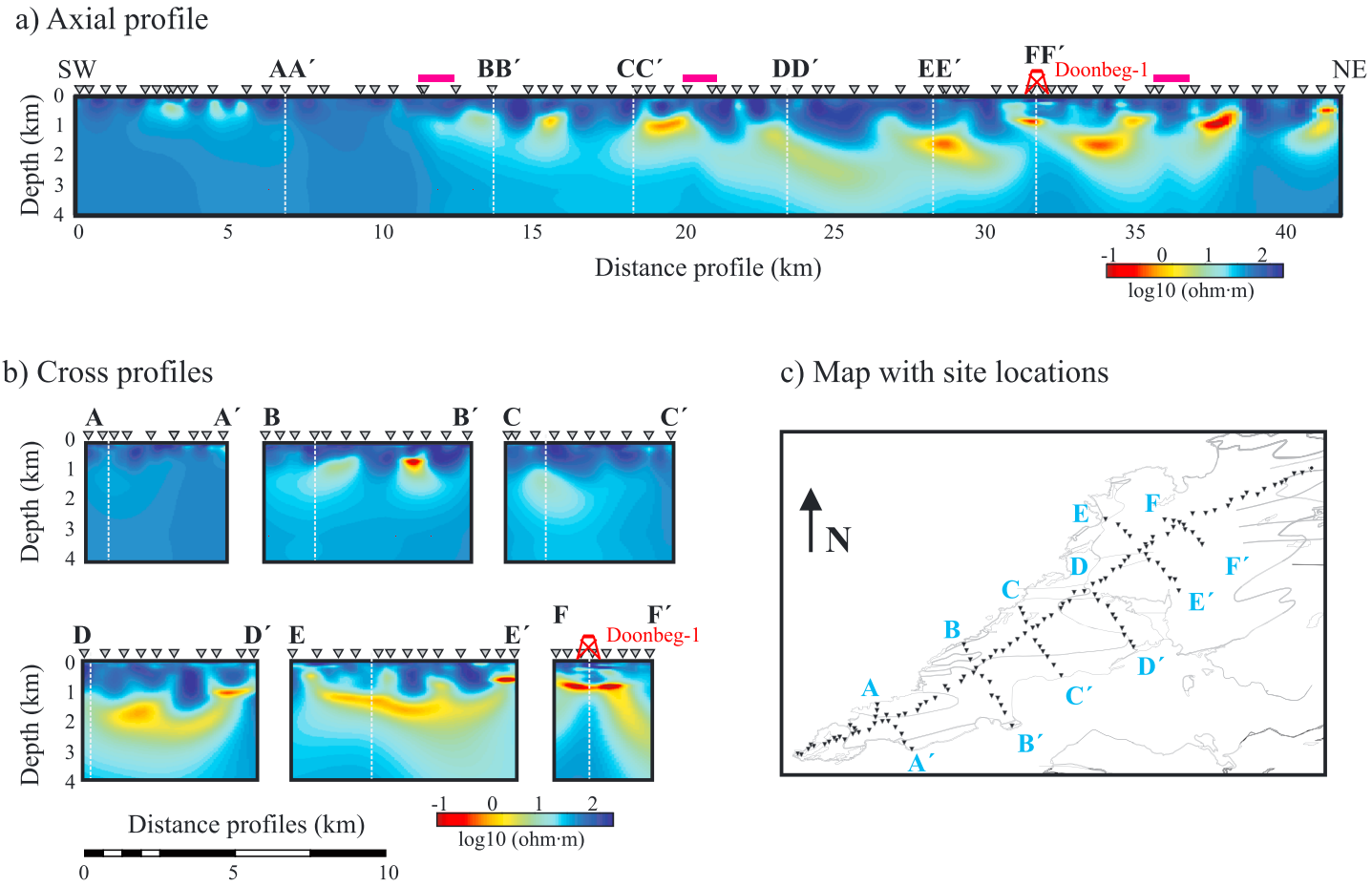

Figure 5. (a) Electrical resistivity model along the longitudinal profile. (b) Electrical resistivity model along the cross profiles. Inverted triangles are the sites where EM data was acquired. AA′-FF′ and white dashed lines indicate the intersection points between longitudinal and cross profiles. Doonbeg-1 well location is indicated in red on top of the electrical resistivity models. Pink horizontal bars on top of MT sites indicate the regions where average between models was applied. (c) Map with the location of the longitudinal and cross profiles.

Finally, Figure 4c shows the agreement between the electrical resistivity data from Doonbeg-1 well (black line) and the electrical resistivity values resulted from the inversion model beneath the well site (red line). Due to the size of the cells and the resolution of the EM methods, the general trend is well captured, but the presence of thin layers with sharp contrasts in resistivity observed from Doonbeg-1 well data is not resolved. The shielding effects caused by the strong conductive layer observed within the lower part of the Clare Shale formation, with electrical resistivity values significantly smaller than 1 Ωm, is observed at depths greater than 1,000 m, where the electrical resistivity model is not capable of imaging the variations observed in the Doonbeg-1 well resistivity profile. Note also that the sensitivity of surface inductive methods is apparent—the MT response represents the depth-integrated conductivity, so thin conductive layers are "smeared" out whereas resistive layers are virtually ignored. Hence, the MT model resistivity lies on the lower limit of the laterolog resistivity. Below 1,000 m, the model has a decrease in resolution and is not able to differentiate layers with different electrical resistivity values.

4.3.3. Results

The results of the inversion process for the four areas were merged into one composite model to facilitate interpretation, logarithmically averaging the resistivity values of the cells shared by the different models. Vertical slices through the final composite model are displayed in Figure 5 showing the electrical resistivity distribution beneath the study area down to 4-km depth. Figure S4 (supporting information) shows the starting model used for the final inversion site by site with the final model presented in Figure 5.

Model resolution decreases significantly (exponentially) in regions away from the profiles where data were acquired. For this reason, we focus only on the results beneath the MT profiles. The vertical white dashed lines in Figure 5 indicate the crossing point between the axial and cross profiles (Figure 1a). The color scale used to represent the electrical resistivity values ranges between 0.1 (dark red) to 500 Ωm (dark blue), because of the significant low electrical resistivity values recovered beneath the area of study.

The final model showed a dominant conductive anomaly that is deeper and more conductive just to the southwest of the Doonbeg-1 well (beneath the cross profiles DD′, and EE′ in Figure 5b) and becomes shallower to the SW and NE. This conductive region is rather heterogeneous and shows significant variations along the profile, with resistivity values ranging between 0.1 and 50 Ωm. From the top of this conductive region up to the surface, higher electrical resistivity values, with local sharp/discrete conductivity anomalies, are identified. Beneath the dominant conductive region, in the lower part of the model, there is also an increase in resistivity, although values are not as high as those observed for the top resistive region. Although the apparent resistivity and phases already suggest an increase in resistivity for longer periods (Figure 3), care needs to be taken when interpreting this lower region because of the decrease in resolution due to the shielding effects caused by the dominant conductive layer (e.g., Figure 4c). It is also worth mentioning that the SW end of the Loop Head Peninsula show significant differences from the rest of the area. In this region, the dominant conductive layer is detached from the rest of the model, occurs at shallower depths, and is significantly reduced in thickness and conductivity.

5. Joint Interpretation

The characterization of the subsurface geology by means of $\boldsymbol{Z}$, $\boldsymbol{T}$, and $\boldsymbol{H}$ is dominated by the diffusion equation, thus providing a relatively fuzzy image of the true electrical resistivity distribution at depth. This makes the interpretation of the results challenging, particularly when comparing data sets with different levels of resolution. Joint interpretation of the Doonbeg-1 well petrophysical data, including electrical resistivity data, was performed to enhance the interpretation of the electrical resistivity model presented in Figure 5. Two main steps were employed: (1) multivariate statistical analysis of Doonbeg-1 well data in order to define major representative groups with similar petrophysical properties and (2) propagation of these representative groups through the electrical resistivity model, based on the representative electrical resistivity values for each group defined in step 1.

5.1. Multivariate Statistical Analysis of Doonbeg-1 Well Data

Multivariate statistical analysis of the Doonbeg-1 well-log data was performed using the sonic velocity, gamma ray, neutron porosity, and electrical resistivity logs. As the depth of resolution of the electrical resistivity model at the well site does not extend deeper than 1,250 m (Figure 4c), we only used data down to 1,250-m depth from the well (Figure 2).

The first step was to normalize the data sets to facilitate comparison between them following equation (1).

$$\check{X}_{ij} = \frac{X_{ij} - \mu_j}{\sigma_j} \tag{1}$$

where $\check{X}$ is the normalized data, X is the measured data, μ the mean value, and σ is the standard deviation. Subindex i indicates the data point (in our analysis values at different depths), and the subindex j the data type (in our analysis sonic transit velocity, neutron porosity, gamma, or electrical resistivity).

The clusters were defined using the expectation-maximization algorithm (Dempster et al., 1977) using the gmdistribution.fit Matlab function. Assuming that the data can be described by a Gaussian mixture model with k components (each of them with assigned parameters, i.e., mean and covariance), the algorithm clusters the data by maximizing the overall probability (i.e., data likelihood). For each number of clusters, the process was repeated several times, each time with a new set of initial parameters randomly selected. The solution with the largest likelihood was returned.

The number of clusters into which to divide the data was selected following two different approaches: (1) Silhouette (Rousseeuw, 1987) and (2) Hierarchical cluster analysis (HCA; Rokach & Maimon, 2005). Silhouette ranges between −1 and +1 and values close to one indicates that the object is well matched to

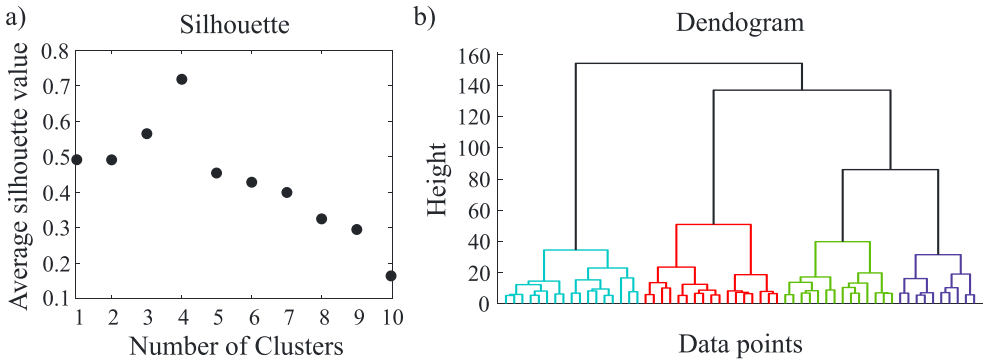

Figure 6. (a) Results from the Silhouette analysis at evaluating the number of groups in which to divide the data from Doonbeg-1 well. Values close to one indicates that the object is well matched to its own cluster and poorly matched to neighboring clusters. (b) Dendrogram showing the result of the Agglomerative HCA performed with Doonbeg-1 well data grouping depths with similar physical properties. Colors divide the data in four groups.

its own cluster and poorly matched to neighboring clusters. The analysis was performed with different numbers of clusters, suggesting that four clusters was the most appropriate for our data (Figure 6a). The HCA approach seeks to build a hierarchy of clusters and to classify naturally occurring subgroups within a data set based upon similarities between the observations. Agglomerative HCA (Euclidean distance and Ward's linkage method) was performed for the Doonbeg-1 well-log data grouping depths with similar petrophysical properties and results plotted as a dendrogram (Figure 6b). Visual examination of the dendrogram suggests the presence of four clusters, distinguished by different colors, consistent with the results from the Silhouette analysis.

Having determined the number of clusters for the well-log data from Doonbeg-1, each depth was assigned to a particular cluster (cA, cB, cC, or cD) based on the gmdistribution.fit Matlab function. Color points in Figure 7a show which cluster the well-log data belong to across the range of depths investigated. Figure 7 b1 shows the main properties of each cluster plotting each petrophysical variable (*y* axis) in relation to the log10 electrical resistivity values (*x* axis). Cluster cA, at shallower depths, is quite well defined for all petrophysical properties, with even a coherent linear relationship between sonic velocity and electrical resistivity values. Figure 7b2 shows the distribution of the electrical resistivity values within each cluster as histograms. The bin width for the histograms, 0.15 at log10 scale, was selected based on the resolution achieved when constraining the subsurface electrical resistivity values using electromagnetic geophysical methods from a synthetic study similar to the model derived from the present study (Campanyà et al., 2016; Table 1). These histograms underpin the interpretation of the electrical resistivity model of Figure 5.

Although clusters cB and cD do not have the same electrical resistivity distribution, these two clusters have overlapping electrical resistivity values, which means that they cannot be differentiated when constraining the electrical resistivity distribution of the subsurface. Figure 7b1 shows that the main difference between these two clusters is observed in the Neutron porosity data, but no major differences are observed when considering the electrical resistivity values. Therefore, to avoid possible misinterpretation, these two clusters were combined.

As a result of this evaluation we defined three major groups with particular electrical resistivity signatures (Figure 7b2). Group 1 was directly related to the cluster cA, showing relatively high electrical resistivity values, above 100 Ωm, and associated with regions with low presence of clay/shale. Group 2 was created from the combination of clusters cB and cD. This group was characterized by electrical resistivity values between 0.8 and 100 Ωm and was associated with regions with presence of clay/shale. Finally, Group 3 was related to the subgroup cC, having very low electrical resistivity values (significantly smaller than 1 Ωm), and related to shale with significant amounts of organic carbon, high organic maturity levels and/or common pyrite.

5.2. Propagation of the Main Groups Along the Electrical Resistivity Model

The electrical resistivity model of the study area (Figure 5) was simplified by replacing the electrical resistivity values of each cell by one of the three groups defined above (Figure 7c). This was performed for three

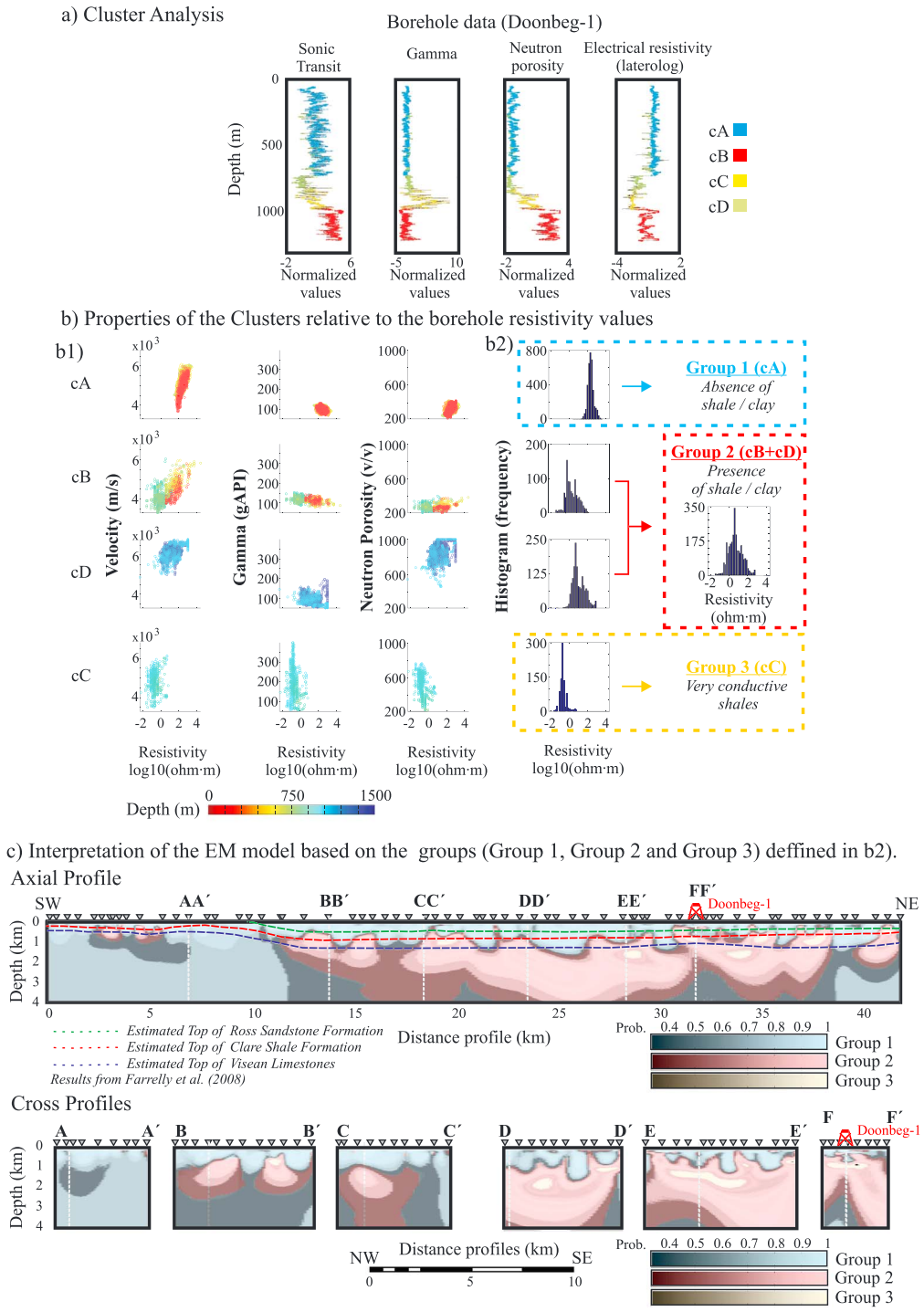

Figure 7. Interpretation of the MT model based on well-log data by means of multivariate statistical analysis. (a) Results from cluster analysis of Doonbeg-1 well assuming four different clusters (cA blue, cB red, cC yellow, and cD green). Note that values were normalized for each type of data. (b) Properties of the clusters relative to the resistivity values. (b1) For each of the cluster in Figure 7a, plot of the physical properties relative to electrical resistivity values. In this case color scale is related to the depth of the samples. (b2) Histogram of the distribution of the resistivity values within the clusters from Figure 7a. Dashed rectangles show the final groups (1, 2, and 3), with different signatures in the distribution of the electrical resistivity values that were used to interpret the EM model. Note that because cB and cD present similar electrical resistivity values these two clusters were joined in Group 2. (c) Interpretation of the EM model based on the groups of clusters defined in b2. Each cell of the EM model in Figure 5 was associated to one of the three groups depending on the electrical resistivity value of the cell. Doted lines are seismic interfaces from the seismic profiles interpreted by (Farrelly et al., 2008). Gray scale superimposed to the model indicates how well the cell fits within the group. Clear areas are well-defined regions and dark areas are poorly defined regions. AA′-FF′ and white dashed lines indicate the intersection points between longitudinal and cross profiles. Doonbeg-1 well location is indicated in red on top of the electrical resistivity models. EM = electromagnetic.

reasons: (1) to simplify the electrical resistivity model, (2) to reduce the influence of the chosen color scale, and (3) to relate the electrical resistivity model to the petrophysical information from the Doonbeg-1 well. Note that to perform this step, the histograms from Figure 7b2 were used to relate the electrical resistivity values of the geophysical model to the Doonbeg-1 well data. The columns of each histogram were divided by the total number of points in each group, thus avoiding issues associated with different numbers of data points defining each group. For a particular electrical resistivity value within the geoelectrical model, the group with a higher column related to this particular resistivity value was selected.

For each cell, we also calculated the probability of being in the selected group and not in the other two groups. This was computed by dividing the height of the histogram of the selected group by the sum of the heights of the histograms of the three groups for this particular electrical resistivity value. The probability of being in the selected group was represented by the gray scale model superimposed on the simplified model of groups with similar electrical resistivity values (Figure 7c), being dark areas of low probability and white transparent areas of high probability.

5.3. Nonlinear Sensitivity Test

The need of Group 3 to explain the data was evaluated by performing a nonlinear sensitivity test. The test consisted in increasing the electrical resistivity values of Group 3 to be comparable to Group 2. In particular, the electrical resistivity values of Group 3 were increased to the minimum electrical resistivity values of Group 2 (~0.5 Ωm), considering only electrical resistivity values where probability of been in Group 2 is larger than been in Group 3. The forward responses before and after this alteration were evaluated following equivalent analysis such as in Meqbel et al. (2014), looking at changes in the nRMS (Figure S5, supporting information). In most of the cases, the nRMS values for the sites around Group 3 increased after the alteration suggesting that the presence of Group 3 is necessary to fit the data. Sites located around Doonbeg-1 well were the most sensitive to Group 3. Moving to the south-west, beneath profiles EE′, DD′, and CC′, the sensitivity decreases, probably because there is a slightly thicker layer of Group 2 above Group 3, and/or because Group 3 is located at greater depths. Finally, the sensitivity test showed that our data is not very sensitive to small clusters of Group 3, and care needs to be taken when considering them. The sensitivity test also showed that $\boldsymbol{Z}$ is the most sensitive data set to Group 3 and that $\boldsymbol{H}$ is more sensitive to Group 3 than $\boldsymbol{T}$.

6. Discussion

The multivariate statistical analysis of the well-log data from Doonbeg-1 highlighted three major groups with particular electrical resistivity values (Figures 7b2). These groups were not coincident with the main stratigraphic units and were mostly related to the presence and absence of clay/shale and to the properties of the shale, including maturation levels of the organic carbon within the shale and/or levels of pyritization. Broadly, the defined groups have allowed us to differentiate between regions where (1) clay/shale is absent, (2) significant amounts of clay/shale is present, and (3) clay/shale associated with very low electrical resistivity values. These three groups were also propagated along the basin using the 3-D electrical resistivity model (Figure 7c).

Prior to discussing the results, two points should be considered when interpreting the grouped electrical resistivity model. First, the model of groups (Figure 7c) is based on the groups with similar petrophysical properties defined at the location of the Doonbeg-1 well. We recognize that away from the well there may be geological units or evidence for geological processes that are not present in the vicinity of Doonbeg-1 but that may have similar electrical resistivity values to the clusters defined in the multivariate statistical analysis. Second, the presence of clay or shale within the shallower section above the Clare Shale Formation may result in vertically elongated conductors in the geoelectrical model connecting the shallower clay/shale layers to the Clare Shale Formation. Campanyà et al. (2015) showed that a significant decrease of resolution is to be expected when constraining high-electrical resistivity structures surrounded, top and bottom, by conductive layers; the study highlighted the influence of the bottom conductive layer in particular. Therefore, although low-electrical resistivity anomalies are expected within the shallower formations, their vertical elongation could be an artefact caused by the lack of resolution of the geophysical method.

Taking these issues into consideration, we focus on the dominant geoelectrical structures within the study area and the implications for a better understanding of this part of the Clare Basin in the subsurface. A

more detailed analysis of particular areas in the model would require the acquisition of more electromagnetic data with a higher density of stations and a new borehole or two (or three) to provide lithological control. To facilitate comparison with other data sets, the top of the main formations defined by Farrelly et al. (2008) were superimposed onto the interpretation of the geoelectrical model (Figure 7c, dotted lines). In Figure 8, we superimposed those regions where clay/shale is present (with a probability greater than 0.5 of being in Groups 2 or 3) on top of the topography, geological, and gravity maps of the survey area.

6.1. Electrical Resistivity Values of Groups 1, 2, and 3

Groups 1 and 2 have peak resistivity values of around 170 Ωm (between 75 and 400 Ωm) and around 7 Ωm (between 0.3 and 125 Ωm), respectively. The limits of the resistivity values were defined by assuming a Gaussian distribution and selecting $\pm 2\sigma$, where σ is the standard deviation. Resistivity values for Group 1 lie within the expected resistivity values associated with sedimentary rocks, and values for Group 2 are in agreement with the common resistivity values assigned to shales (Chave et al., 2012; Haak & Hutton, 1986). The large range of resistivity values observed in Group 2 occurs because this group comprises regions where shale is present together with other sedimentary rocks that influence the bulk electrical resistivity values of this group. In Figure 7b, although there is an overlap in resistivity between clusters cB and cD, cluster cD, which is related to the presence of shale within limestones, is somewhat more resistive than cluster cB, which is associated with shales within the shallower rock units that are mainly sandstones, siltstones, and mudstones.

The electrical resistivity values of Group 3, with peak resistivity around 0.15 Ωm (between 0.06 and 0.40 Ωm), are significantly lower than the typical values related to shale or any other sedimentary rock. Significant amounts of organic carbon within a shale can modify the observed bulk resistivity, depending on the thermal maturity stage. Electrical resistivity values of organic carbon can range from above 10^6 Ωm for low rank maturity (the oil window) to values of between 10^0 and 10^{-2} Ωm for the anthracite and meta-anthracite maturation zones, to even more conductive values for the graphite and semi-graphite zones (Parkhomenko & Keller, 1967; Teichmüller et al., 1979). The presence of organic carbon within the meta-anthracite maturity zone observed in the Doonbeg-1 well is in agreement with the electrical resistivity values associated with Group 3 at similar depths. This suggests that in this particular case the EM geophysical data are able to identify regions in which these types of shale are present in relatively abundant quantities. Although the presence of organic carbon within the shale in meta-anthracite form can explain the observed resistivity values, the presence of pyrite observed within the Clare Shale Formation could also contribute to the observed low electrical resistivity values.

6.2. Spatial Distribution of Groups 1, 2, and 3

Figure 7c shows that Group 1 is located at shallower depths than the other groups, with greater thicknesses present between Cross Profiles D and E and thinning to the NE and SW toward the edges of the model due to shallowing of the base of the clastic succession. The interfingering of Groups 1 and 2 at shallower depths seems to increase to the N-NE, particularly around Cross Profile FF′ and sites further to the NE. As Group 2 is thought to identify shale, this spatial distribution of Group 2 is in agreement with the hypothesis that during deposition of the Ross Sandstone Fm, the area to the north stood structurally higher with shale deposit persisting in north Clare. As no thinning of the Ross Sandstone Fm is evident from the model, the interfingering of Groups 1 and 2 may record muddy slump units interleaved with the basin floor sandstones in a base of slope position. The slumps may have been shed from the confining slope separating the area of condensed (and thin) shale deposition to the north from the basin floor system in the south. Southwest of Cross Profile B, Group 1 is quite dominant with significantly high probability values at all depths. As mentioned before, as the SW part of the study area is far from the Doonbeg-1 well, we suspect that different geological units may be present here, particularly at depths greater than 1 km. Thus, it is prudent that this area should not be interpreted by assuming that the top formations beneath Doonbeg-1 reach greater depths to the SW of the Loop Head Peninsula.

Group 2 mostly underlies Group 1. Figures 5 and 7c show that the more conductive regions of the model related to Group 2 are thicker and deeper beneath Cross Profiles DD′, EE′, and FF′ and tend to narrow and occur at shallower depths toward the edges of the Axial profile. At the SW end of the Axial Profile

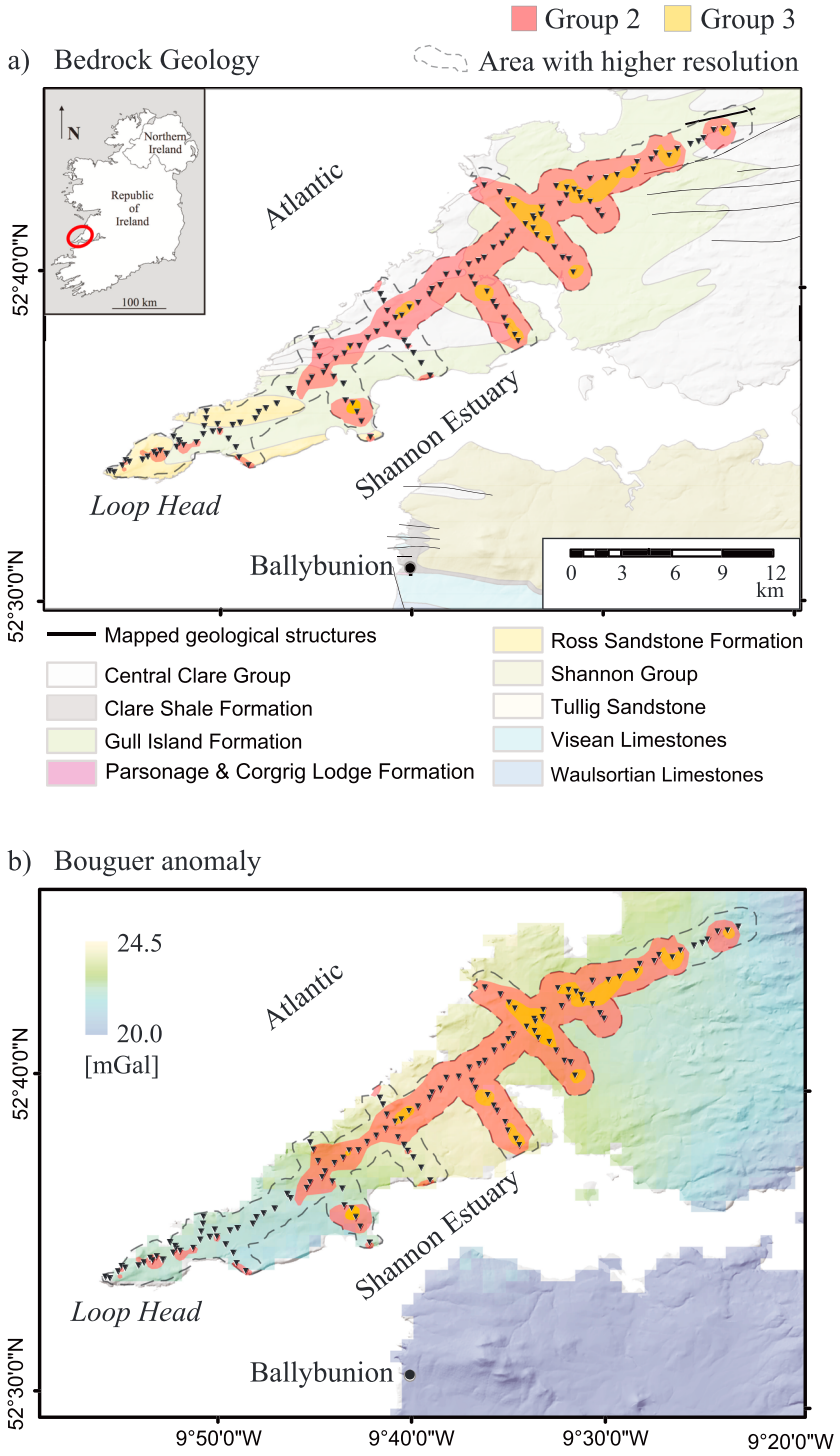

Figure 8. (a) Geological and (b) Bouguer anomaly maps. Superimposed the areas with probability larger than 0.5 to be in Group 2 (presence of shale) or Group 3 (very conductive shale). Halo (black dashed lines) defines the area with reliable resolution from the MT model based on results from synthetic data (Campanyà et al., 2016).

(Figure 7c), Group 2 seems to terminate abruptly between Cross profiles AA′ and BB′. Further to the SW near Loop Head, only a few shallow and thin regions of Group 2 are observed.

Group 3 (yellow regions in Figures 7c and 8) is located within Group 2 but is quite scattered and shows no clear continuity. The distribution of Group 3 shows that the very conductive shales are more abundant close

to the Doonbeg-1 well. This result does not reject the possibility of finding these types of shales in other areas but suggests that in the region of Doonbeg-1 there is higher probability of finding them in greater amounts. The absence of a continuous layer associated with Group 3 can be explained if the high maturation levels were caused by heating by advecting fluids (Fitzgerald et al., 1994; Goodhue & Clayton, 1999). Occurrences of Group 3 could thus relate to local pathways used by deep and old hydrothermal systems responsible for the elevated temperatures (in excess of 300 °C), which caused the overmaturation of the organic content within the shales. Note that the very conductive shales are mostly observed beneath Cross Profiles EE′ and FF′ in Figure 7c and are less common in the SW of the Loop Head Peninsula, which could suggest that the hydrothermal activity was stronger in the NE part of the studied area. A higher degree of heating in the NE part of the study area would thus provide lower electrical resistivity values associated with the shale in this region than in the SW end of the Loop Head Peninsula. The hypothesis of fluid advective heating is also consistent with the VR data from the Doonbeg-1 well, which show that the maturation levels do not always increase with depth, and instead have a more complex profile with an apparent reverse gradient in the upper part of the Viséan Limestones near the base of the Clare Shale Formation. The results in Figures 7 and 8 provide support for the hypothesis of fluid advective heating and are less supportive of other hypotheses such as simple burial metamorphism to explain the elevated temperatures that affected the organic carbon within the shale. Other hypothesis, such as (1) hydraulic fractionation of the organic components with concentration of organic matter and (2) tectonic uncoupling on the Clare Shale during Variscan deformations, cannot be discarded when explaining the disrupted continuity of the mechanically weak "hot" part of the shale with its abundant condensed sections.

The model with petrophysical groups of similar electrical properties was compared with the top of the main lithological units defined by Farrelly et al. (2008) in Figure 7c. Dark blue dashed lines indicate the top of the Viséan Limestones, red dashed lines indicate the top of the Clare Shale Formation, and green dashed lines indicate the top of the Ross Sandstone Formation. It is important to note that Farrelly et al. (2008) defined the top of the main lithological units based on results from 2-D seismic reflection profiles, whereas the new electrical resistivity model defines regions with and without shale content, as well as some of the properties of the shale, which are properties that are poorly constrained to totally unconstrained by seismic data. Comparison between our results with the top of the main lithological units show no clear correlation, in part because the presence of shale is not only constrained within the Clare Shale Formation, but also within shallow and deeper formations. Only Group 3 seems to be relatively well constrained within the seismic boundaries for the Clare Shale Formation, between the red and dark blue dashed lines in Figure 7c, although these results differ at the deepest parts of the basin beneath Cross Profiles D and E. In addition, above the top of the Ross Sandstone Formation (green dashed line), Group 1 appears to be dominant along the whole profile, particularly SW of Doonbeg-1.

In general, the EM model suggests a far more complex geometry than that proposed by Farrelly et al. (2008). However, there are significant agreements between the two data sets including the constraint of the deepest parts of the basin SW of Doonbeg-1 well and the rise to shallower depths of the main units at the SW end of the study area at Loop Head (between Cross Profiles AA′ and BB′; Figure 7c).

Gravity data show larger Bouguer anomaly values (Figures 1 and 8, warm colors) associated with the deepest part of the basin in the central part of the Loop Head Peninsula, and the values decrease toward the edges of the model, suggestive of a thinning of the preserved basin fill. Farrelly et al. (2008) suggested that changes in Bouguer anomaly are probably related to unseen dense basement, thus the relationship between changes in Bouguer anomaly and depth of the basin are causal. Data currently collected by the Tellus project (www.tellus.ie) may help explaining why the high values of the Bouguer anomaly are related to the deepest parts of the basin and if there is any influence from the basin sediments or if is all related to the basement.

When comparing our models with gravity data, areas with present shale (Groups 2 and 3) are, in general, coincident with higher Bouguer anomaly values (Figure 8b). Note, however, that some discrepancies are observed in the region between Cross Profiles BB′ and CC′. Bouguer anomaly values are similar to the values observed beneath the Doonbeg-1 well, but an EM-based interpretation suggests that the thickness of Groups 2 and 3 is smaller between Cross Profiles BB′ and CC′ than beneath the Doonbeg-1 well. This discrepancy could be related to a decrease in shale content or a decrease in the amount of organic

matter between BB′ and CC′. An alternative interpretation assuming differences in the properties of the organic carbon would suggest that the shales between Cross Profiles BB′ and CC′ were less affected by the high temperatures that affected Doonbeg-1, thus obtaining higher electrical resistivity values than in the NE part of the model.

Finally, the low Bouguer anomaly values observed between Cross Profiles AA′ and BB′ coupled with the absence of shale in this area suggest a significant thinning of the preserved clastic basin fill (Figure 8), which is in agreement with the shape of Group 2 in this region (Figure 7c) and the results from Farrelly et al. (2008). Note however, that further to the SW the Bouguer anomaly values increase slightly and the presence of significant amounts of shale reappear although in small amounts. This region between Cross Profiles AA′ and BB′, with the lowest Bouguer anomaly values in the Peninsula and with higher electrical resistivity values than the surrounding area, divides the Loop Head Peninsula by separating the deepest part of the basin constrained by the Doonbeg-1 data and a small and less well-constrained region observed at the SW end of the Loop Head Peninsula. The absence of clay/shale in this region between Cross Profiles AA′ and BB′, although it may be related to a discontinuity in the basin, could also be caused by the presence of shale with organic content at lower maturity levels than beneath Doonbeg-1. Note, however, that care should be taken when interpreting the SW end of the Loop Head Peninsula based on the analysis from the Doonbeg-1 well, where a different and more complex geological environment is expected from the results of this study.

6.3. Implications for CO_2 Storage and Geothermal Energy

Several recent and existing studies and projects highlight current interest in the Clare basin as a potential site for both CO_2 storage and geothermal energy (i.e., IRETHERM, IRECCSEM, and HOTLIME). A detailed analysis from Farrelly et al. (2008) evaluated the potential for CO_2 storage in saline aquifers in the Ross Sandstone Formation and in the Viséan Limestones. Their study concluded that these lithologies are not suitable for CO_2 storage, mainly due to (1) small aquifer size and (2) extremely low permeability and porosity values from point well-log data (i.e., the Doonbeg-1 well). In other regions, EM models have shown to be valuable for constraining porosity values in sedimentary basins (e.g., Meqbel et al., 2013). However, the presence of disseminated clay and shale in most of the geological formations in the Clare Basin make it difficult to undertake a reliable analysis, as the contrast in resistivity related either to changes in porosity and permeability will be masked by the presence or absence of clay/shale.

The Clare Shale Formation could present another option for CO_2 storage if a significant reservoir of either gas or oil was present. A review by Khosrokhavar et al. (2014) examined the potential for CO_2 storage in shale, and there exists the additional potential of using CO_2 for enhanced gas recovery by hydraulic fracturing (e.g., Tao & Clarens, 2013). In the particular case of the Clare basin, the region around the Doonbeg-1 well was strongly affected by hot fluids that produced high maturity levels in the organic content. However, results from this study (Figures 7 and 8) suggest that the influence of the hot fluids was less important in the SW part of the basin. This suggests that lower maturity levels would be expected in this region of the basin, which would make this area more suitable for CO_2 storage. Note however, that the general the lack of potential large reservoirs and the presence of faults along the Clare basin (Farrelly et al., 2008) discourage the use of the whole basin for CO_2 storage. CO_2 storage in the basin may not be economically profitable, and the risk of instability in the reservoir is high. In addition, the Prohibition of Onshore Hydraulic Fracturing Bill (Petroleum and Other Minerals Development, Act 2017, No 15, https://data.oireachtas.ie/ie/oireachtas/act/2017/15/eng/enacted/a1517.pdf) has made it illegal to extract onshore petroleum (including shale gas) by hydraulic fracturing in Ireland (Statutory Instrument No. 15 of 2017).

On the other hand, the basin has good potential for geothermal energy. SLR (2011) assigned the Clare basin a low risk status for geothermal energy development because of the presence of insulating shale and the possibility of deep fractures to provide hydraulic conductivity. In addition, several authors have reported on relatively high heat flow from the basin (e.g., Brock, 1989; Fullea et al., 2014; Goodman et al., 2004; Jones et al., 2014) with temperatures expected to be at least 70 °C at 2.5-km depth. The uraniferous Clare Shale Formation has been identified by Willmot Noller et al. (2015) as having the highest heat production rate of any exposed bedrock in Ireland. As such, the shales may provide a good target for an enhanced geothermal system where they exist in sufficient thickness at depth (270-m thick at

Doonbeg-1). The presence of high temperatures at accessible depths makes the Clare basin suitable for large-scale geothermal heating projects (e.g., Lund et al., 2014), providing of course that sufficient permeability can be found in the reservoir. The results of this study support the presence of deep fractures that must once have been pathways for a deep hydrothermal system, as evidenced by the maturation history of the basin. These fractures could be suitable for future use as an enhanced geothermal system, particularly in the region where our Group 3 parameters are observed in Figures 7 and 8, mostly around the Doonbeg-1 well.

7. Conclusions

The integration of well-log and EM geophysical data has contributed to a better understanding of the Clare basin, providing new constraint about (1) the geology beneath the west Clare, (2) the large-scale stratigraphic architecture, and (3) the geological evolution. The EM model suggests a more complex geological environment than previous studies inferred, showing significant agreement with the previous interpretations based on seismic and gravity data at imaging: (1) the deepest part of the preserved basin fill succession SW of the Doonbeg-1 well and (2) the rise to shallower depths of the main units at the SW end of the Loop Head Peninsula, between Cross Profiles AA′ and BB′.

Multivariate statistical analysis successfully classified the sedimentary rocks encountered in the Doonbeg-1 well into three major groups with definitive electrical resistivity signatures: (1) Group 1 was associated with sedimentary lithologies such as sandstones, siltstones, and mudstones in units devoid of, or with low abundances of, clay/shale, and has electrical resistivity values of around 170 Ωm (between 75 and 400 Ωm); (2) Group 2 was related to areas where clay/shale is present, with average resistivity values around 7 Ωm (between 0.3 and 125 Ωm); and (3) Group 3 was associated with shale occurrences with a significant presence of organic carbon at a high maturity stage and presents typical resistivity values of around 0.15 Ωm (between 0.06 and 0.4 Ωm). Propagation of the groups along the basin was compared with the top of the main formations showing that the presence of clay/shale is observed within most of the formations and not restricted within the Clare Shale Formation. The only group that appears to correlate well with any of the main stratigraphic units is Group 3, which coincides with the Clare Shale Formation, although some discrepancies were observed, particularly at the deepest parts of the basin, to the SW of Doonbeg-1.

Superposition of Groups 2 and 3 on top of the gravity map showed two regions with significant differences with the rest of the basin: (1) between Cross Profiles BB′ and CC′, the gravity data suggest similar thickness of sedimentary rocks to those beneath Doonbeg-1, but the relative amount of clay/shale between the two regions seems to disagree. This could be related to a decrease of clay/shale and organic carbon within the sediments between cross profiles BB′ and CC′ and/or to a decrease in the maturation levels of the organic carbon within the shale between BB′ and CC′; and (2) the low Bouguer anomaly values between Cross Profiles AA′ and BB′ is coincident with an increase in resistivity from the EM model, and with the absence of Groups 2 and 3, suggesting a possible discontinuity within the basin separating the main part of the basin to the NE from the region at the SW end of the Loop Head Peninsula. Although more data would be required to support this hypothesis, the high electrical resistivity values and the lack of Groups 2 and 3 observed between Cross Profiles AA′ and BB′ could be related to a change in the physical properties of the organic carbon within the shale, that is, if it was of a lower maturity stage.

Finally, the distribution of Group 3, which is sparsely distributed but mostly concentrated around Doonbeg-1, supports the hypothesis of fluid advective heating to explain the high maturity levels observed in Doonbeg-1 well. Under this hypothesis, Group 3 would be related to significant amounts of organic carbon that was affected by an old and hot (in excess of 300 ^{o}C), structurally facilitated hydrothermal system responsible for the over-maturation of the organic carbon. The distribution of Group 3 close to Doonbeg-1 does not preclude the influence of hot fluids in other regions of the basin, but does suggest that the region in the NE of the basin was more affected by hydrothermal fluids and fluid advection heating and maturation than the SW part of the Loop Head Peninsula. Despite the apparent absence of obvious faults in the basin, the discontinuity of Group 3 suggests a significantly fractured basin, imaging fractures that were once used by an old and hot (>300 °C) geothermal system. The presence of these deep fractures in a region with

relatively high head flow and with the presence of insulating shale supports the use of the Clare Basin as a potential site for geothermal energy but not for the storage of CO_2.

Acknowledgments
We would like to acknowledge the financial support to J. C. and X. O. from the IRECCSEM project (www.ireccsem.ie) funded by a Science Foundation of Ireland Investigator Project Award (SFI: 12/IP/1313) to A. G. J. Gary Egbert, Anna Kelbert, and Naser Meqbel are very gratefully thanked for making their ModEM code available to the community. The authors wish to acknowledge Irish Centre for High-End Computing (ICHEC) for the computing facilities provided, and the Petroleum Affairs Division of the Department of Communications, Climate Action, and Environment for providing the Doonbeg-1 well-log data. We would like to thank the fieldwork assistants: Ashten Sawitsky, Caitriona Keogh, Keith Galvin, and Stephen P. Coakley for their help at acquiring MT data. EM data from the project is available in https://figshare.com/s/90bfb6de16057f355131 website. Well-log data is not publicly available but can be accessed by contacting Petroleum Affairs Division of the Department of Communications, Climate Action, and Environment in Ireland.

References

Berdichevski, M. N., & Dmitriev, V. I. (2008). *Models and Methods of Magnetotellurics*. Berlin: Springer. https://books.google.ie/books?id=-Fs8cPqeCcQC&pg=PA4&lpg=PA4&dq=Berdichevsky+and+dimitriev&source=bl&ots=2CaMxmL08v&sig=YvJ--LgFPQip0ztNAMQAuN5l1KY&hl=ca&sa=X&ved=0ahUKEwijlcj5yebXAhWLKVAKHUwvAWwQ6AEINzAF#v=onepage&q=Berdichevskyanddimitriev&f=false

Berdichevsky, M. N. (1968). *Electrical prospecting by the method of magnetotelluric profiling*. Berlin: Nedra.

Best, J. L., & Wignall, P. B. (2016). *A field guide to the carboniferous sediments of the Shannon Basin*. Western Ireland: Wiley-Blackwell. http://www.wiley.com//legacy/wileychi/best/

Blake, S., Henry, T., Muller, M. R., Jones, A. G., Moore, J. P., Murray, J., et al. (2016). Understanding hydrothermal circulation patterns at a low-enthalpy thermal spring using audio-magnetotelluric data: A case study from Ireland. *Journal of Applied Geophysics*, *132*, 1–16. https://doi.org/10.1016/j.jappgeo.2016.06.007

Braithwaite, K. (1993). Statigraphy of a mid-carboniferous section at Inishcorker, Ireland. *Annales de La Societe Geologique de Belgique*, *116*(2), 209–219.

Brock, A. (1989). Heat flow measurements in Ireland. *Tectonophysics*, *164*(2-4), 231–236. https://doi.org/10.1016/0040-1951(89)90016-4

Campanyà, J., Jones, A. G, Vozár, J., Rath, V., Blake, S., Delhaye, R., & Farrell, T. (2015). Porosity and permeability constraints from electrical resistivity models: Examples using magnetotelluric data. In *Proceedings World Geothermal Congress*. Melbourne, Australia. https://pangea.stanford.edu/ERE/db/WGC/papers/WGC/2015/13121.pdf.

Campanyà, J., Ledo, J., Queralt, P., Marcuello, A., & Jones, A. G. (2014). A new methodology to estimate magnetotelluric (MT) tensor relationships: Estimation of Local Transfer-Functions by Combining Interstation Transfer-Functions (ELICIT). *Geophysical Journal International*, *198*(1), 484–494. https://doi.org/10.1093/gji/ggu147

Campanyà, J., Ledo, J., Queralt, P., Marcuello, A., Muñoz, J. A., Liesa, M. L., & Jones, A. G. (2018). New geoelectrical characterization of a continental collision zone in the Central–Eastern Pyrenees: Constraints from 3-D joint inversion of electromagnetic data. *Tectonophysics*, *742-743*, 168–179. https://doi.org/10.1016/J.TECTO.2018.05.024

Campanya, J., Ogaya, X., Jones, A. G., Rath, V., Vozar, J., & Meqbel, N. (2016). The advantages of complementing MT profiles in 3-D environments with geomagnetic transfer function and interstation horizontal magnetic transfer function data: Results from a synthetic case study. *Geophysical Journal International*, *207*(3), 1818–1836. https://doi.org/10.1093/gji/ggw357

Cantwell, T. (1960). *Detection and analysis of low frequency magnetotelluric signals*. Massachusetts: MIT.

Chave, A. D., & Jones, A. G. (1997). Electric and magnetic field galvanic distortion decomposition of BC87 data. *Journal of Geomagnetism and Geoelectricity*, *49*(6), 767–789. https://doi.org/10.5636/jgg.49.767

Chave, A. D., Jones, A. G., Mackie, R., & Rodi, W. (2012). *The magnetotelluric method*. Cambridge: Cambridge University Press. https://doi.org/10.1017/CBO9781139020138

Chave, A. D., & Smith, J. T. (1994). On electric and magnetic galvanic distortion tensor decompositions. *Journal of Geophysical Research*, *99*(B3), 4669–4682. https://doi.org/10.1029/93JB03368

Chave, A. D., & Thomson, D. J. (2004). Bounded influence magnetotelluric response function estimation. *Geophysical Journal International*, *157*(3), 988–1006. https://doi.org/10.1111/j.1365-246X.2004.02203.x

Chew, D. M., & Strachan, R. A. (2014). The Laurentian Caledonides of Scotland and Ireland. *Geological Society, London, Special Publications*, *390*(1), 45–91. https://doi.org/10.1144/SP390.16

de Morton, S. N., Wallace, M. W., Reed, C. P., Hewson, C., Redmond, P., Cross, E., & Moynihan, C. (2015). The significance of Tournaisian tectonism in the Dublin basin: Implications for basin evolution and zinc-lead mineralization in the Irish Midlands. *Sedimentary Geology*, *330*, 32–46. https://doi.org/10.1016/j.sedgeo.2015.09.017

Dempster, A. P., Laird, N. M., & Rubin, D. B. (1977). Maximum likelihood from incomplete data via the EM algorithm. *Journal of the Royal Statistical Society: Series B: Methodological*, *39*(1), 1–22. http://links.jstor.org/sici?sici=0035-9246%281977%2939%3A1%3C1%3AMLFIDV%3E2.0.CO%3B2-Z, https://doi.org/10.1111/j.2517-6161.1977.tb01600.x

Egbert, G. D., & Booker, J. R. (1989). Multivariate analysis of geomagnetic array data: 1. The response space. *Journal of Geophysical Research*, *94*(B10), 14,227–14,247. https://doi.org/10.1029/JB094iB10p14227

Egbert, G. D., & Booker, J. R. (1986). Robust estimation of geomagnetic transfer functions. *Geophysical Journal International*, *87*(1), 173–194. https://doi.org/10.1111/j.1365-246X.1986.tb04552.x

Egbert, G. D., & Kelbert, A. (2012). Computational recipes for electromagnetic inverse problems. *Geophysical Journal International*, *189*(1), 251–267. https://doi.org/10.1111/j.1365-246X.2011.05347.x

Falgàs, E., Ledo, J., Benjumea, B., Queralt, P., Marcuello, A., Teixidó, T., & Martí, A. (2011). Integrating hydrogeological and geophysical methods for the characterization of a deltaic aquifer system. *Surveys in Geophysics*, *32*(6), 857–873. https://doi.org/10.1007/s10712-011-9126-2

Farquharson, C. G., Oldenburg, D. W., Haber, E., & Shekhtman, R. (2002). An algorithm for the three-dimensional inversion of magnetotelluric data. In *SEG Technical Program Expanded Abstracts* 2002, 649–52. Society of Exploration Geophysicists. https://doi.org/10.1190/1.1817336.

Farrelly, I. J., Loske, B., Neele, F. P., & Holdstock, M. P. (2008). Assesment of the potential for geological storage of CO2 in hypothetical deep saline aquifers in the Vicinity of Moneypoint, Co. Clare.

Fitzgerald, E., Feely, M., Johnston, J. D., Clayton, G., Fitzgerald, L. J., & Sevastopulo, G. D. (1994). The Variscan thermal history of West Clare, Ireland. *Geological Magazine*, *131*(04), 545. https://doi.org/10.1017/S0016756800012152

Fullea, J., Muller, M. R., Jones, A. G., & Afonso, J. C. (2014). The lithosphere-asthenosphere system beneath Ireland from integrated geophysical-petrological modeling—II: 3D thermal and compositional structure. *Lithos*, *189*, 49–64. https://doi.org/10.1016/j.lithos.2013.09.014

Gabàs, A., Macau, A., Benjumea, B., Queralt, P., Ledo, J., Figueras, S., & Marcuello, A. (2016). Joint audio-magnetotelluric and passive seismic imaging of the Cerdanya Basin. *Surveys in Geophysics*, *37*(5), 897–921. https://doi.org/10.1007/s10712-016-9372-4

Gamble, T. D. (1979). Error analysis for remote reference magnetotellurics. *Geophysics*, *44*(5), 959–968. https://doi.org/10.1190/1.1440988

Gamble, T. D., Goubau, W. M., & Clarke, J. (1979). Magnetotellurics with a remote magnetic reference. *Geophysics*, *44*(1), 53–68. https://doi.org/10.1190/1.1440923

García-Yeguas, A., Ledo, J., Piña-Varas, P., Prudencio, J., Queralt, P., Marcuello, A., et al. (2017). A 3D joint interpretation of magneto-telluric and seismic tomographic models: The case of the volcanic island of Tenerife. *Computers & Geosciences*, *109*, 95–105. https://doi.org/10.1016/J.CAGEO.2017.08.003

Goodhue, R., & Clayton, G. (1999). Organic maturation levels, thermal history and hydrocarbon source rock potential of the Namurian rocks of the Clare Basin, Ireland. *Marine and Petroleum Geology*, *16*(7), 667–675. https://doi.org/10.1016/S0264-8172(99)00016-1

Goodman, R., Jones, G.L., Kelly, J., Slowey, E., O'Neill, N., (2004). Geothermal energy resource map of Ireland. SEI commissioned report, Dublin, Ireland.

Graham, J. R. (2009). Devonian. In C. H. Holland & L. S. Sanders (Eds.), *The geology of Ireland* (pp. 175–214). Edinburgh: Dunedin Academic Press.

Haak, V., & Hutton, R. (1986). Electrical resistivity in continental lower crust. *Geological Society, London, Special Publications*, *24*(1), 35–49. https://doi.org/10.1144/GSL.SP.1986.024.01.05

Habibian, B. D., Brasse, H., Oskooi, B., Ernst, T., Sokolova, E., & Varentsov, I. (2010). The conductivity structure across the Trans-European Suture Zone from magnetotelluric and magnetovariational data modeling. *Physics of the Earth and Planetary Interiors*, *183*(3–4), 377–386. https://doi.org/10.1016/j.pepi.2010.08.005

Hodson, F. (1953). The beds above the Carboniferous Limestone in north-west County Clare, Eire. *Quarterly Journal of the Geological Society*, *109*(1–4), 259–283. https://doi.org/10.1144/GSL.JGS.1953.109.01-04.11

Information Handling Services (IHS) (2008). Republic of Ireland continental shelf oil well records. Report: Well Number Doonbeg 1.

Jones, A. G., Afonso, J. C., Fullea, J., & Salajegheh, F. (2014). The lithosphere-asthenosphere system beneath Ireland from integrated geophysical-petrological modeling—I: Observations, 1D and 2D hypothesis testing and modeling. *Lithos*, *189*, 28–48. https://doi.org/10.1016/j.lithos.2013.10.033

Jones, A. G. (2011). Three-dimensional galvanic distortion of three-dimensional regional conductivity structures: Comment on 'Three-dimensional joint inversion for magnetotelluric resistivity and static shift distributions in complex media' by Yutaka Sasaki and Max A. Meju. *Journal of Geophysical Research*, *116*, B12104. https://doi.org/10.1029/2011JB008665

Jones, A. G., & Jödicke, H.. (1984). Magnetotelluric transfer function estimation improvement by a coherence-based rejection technique. In *SEG Technical Program Expanded Abstracts 1984*, 51–55. Society of Exploration Geophysicists. https://doi.org/10.1190/1.1894081.

Kelbert, A., Meqbel, N., Egbert, G. D., & Tandon, K. (2014). ModEM: A modular system for inversion of electromagnetic geophysical data. *Computers & Geosciences*, *66*, 40–53. https://doi.org/10.1016/j.cageo.2014.01.010

Khosrokhavar, R., Griffiths, S., & Wolf, K. (2014). Shale gas formations and their potential for carbon storage: Opportunities and outlook. *Environmental Processes*, *1*(4), 595–611. https://doi.org/10.1007/s40710-014-0036-4

Ledo, J., Queralt, P., & Pous, J. (1998). Effects of galvanic distortion on magnetotelluric data over a three-dimensional regional structure. *Geophysical Journal International*, *132*(2), 295–301. https://doi.org/10.1046/j.1365-246x.1998.00417.x

Lund, H., Werner, S., Wiltshire, R., Svendsen, S., Thorsen, J. E., Hvelplund, F., & Vad Mathiesen, B. (2014). 4th Generation District Heating (4GDH): Integrating smart thermal grids into future sustainable energy systems. *Energy*, *68*, 1–11. https://doi.org/10.1016/j.energy.2014.02.089

Martinsen, O. J. (1989). Styles of soft-sediment deformation on a Namurian (Carboniferous) delta slope, Western Irish Namurian Basin, Ireland. *Geological Society*, *41*, 167–177. http://sp.lyellcollection.org/content/41/1/167.abstract, https://doi.org/10.1144/GSL.SP.1989.041.01.13

Martinsen, O. J., Lien, T., Walker, R. G., & Collinson, J. D. (2003). Facies and Sequential organisation of a mudstone-dominated slope and basin floor succession: The Gull Island Formation, Shannon Basin, Western Ireland. *Marine and Petroleum Geology*, *20*(6–8), 789–807. https://doi.org/10.1016/j.marpetgeo.2002.10.001

McDermot, C.C., & Sevastopulo, G.D. (1972). Upper Devonian and Lower Carboniferous statrigraphical setting of Irish mineralization.

Meqbel, N., Ritter, O., & DESIRE Group (2013). A magnetotelluric transect across the Dead Sea Basin: Electrical properties of geological and hydrological units of the upper crust. *Geophysical Journal International*, *193*(3), 1415–1431. https://doi.org/10.1093/gji/ggt051

Meqbel, N., Egbert, G. D., Wannamaker, P. E., Kelbert, A., & Schultz, A. (2014). Deep electrical resistivity structure of the northwestern U. S. derived from 3-D inversion of USArray magnetotelluric data. *Earth and Planetary Science Letters*, *402*, 290–304. https://doi.org/10.1016/j.epsl.2013.12.026

Ogaya, X., Alcalde, J., Marzán, I., Ledo, J., Queralt, P., Marcuello, A., et al. (2016). Joint in Hontomín (Spain). *Solid Earth*, *7*(3), 943–958. https://doi.org/10.5194/se-7-943-2016

Parkhomenko, E. I., & Keller, G. V. (1967). *Electrical properties of rocks*. US: Springer. https://books.google.ie/books?hl=ca&lr=&id=NTfrBwAAQBAJ&oi=fnd&pg=PA2&dq=Electrical+Properties+of+Rocks&ots=_jwNlie-ci&sig=MUDku3Yb3btcHePXNXkCaM99GaU&redir_esc=y#v=onepage&q=Electrical Properties of Rocks&f=false, https://doi.org/10.1007/978-1-4615-8609-8

Parkinson, W. D. (1962). The influence of continents and oceans on geomagnetic variations. *Geophysical Journal International*, *6*(4), 441–449. https://doi.org/10.1111/j.1365-246X.1962.tb02992.x

Pierce, C. S., Haughton, P. D. W., Shannon, P. M., Pulham, A. J., Barker, S. P., & Martinsen, O. J. (2018). Variable character and diverse origin of hybrid event beds in a sandy submarine fan system, Pennsylvanian Ross Sandstone Formation, Western Ireland. *Sedimentology*, *65*(3), 952–992. https://doi.org/10.1111/sed.12412

Prohibition of Onshore Hydraulic Fracturing Bill (2017). Petroleum and Other Minerals Development, Act 2017, No 15. https://data.oireachtas.ie/ie/oireachtas/act/2017/15/eng/enacted/a1517.pdf

Pyles, D. R. (2008). Multiscale stratigraphic analysis of a structurally confined submarine fan: Carboniferous Ross Sandstone, Ireland. *AAPG Bulletin*, *92*(5), 557–587. https://doi.org/10.1306/01110807042

Rider, M. H. (1974). The Namurian of West County Clare. *Proceedings of the Royal Irish Academy. Section B: Biological, Geological, and Chemical Science*. https://doi.org/10.2307/20518942

Rokach, L., & Maimon, O. (2005). Clustering methods. In *Data Mining and Knowledge Discovery Handbook*, (pp. 321–352). New York: Springer-Verlag. https://doi.org/10.1007/0-387-25465-X_15

Rokityanski, I. I. (1961). On the application of the magnetotelluric method to anisotropic and inhomogeneous masses. *Izvestia*, *11*, 1607–1613.

Rousseeuw, P. J. (1987). Silhouettes: A graphical aid to the interpretation and validation of cluster analysis. *Journal of Computational and Applied Mathematics*, *20*, 53–65. https://ac.els-cdn.com/0377042787901257/1-s2.0-0377042787901257-main.pdf?_tid=b56acfdc-d682-11e7-b0dc-00000aab0f26&acdnat=1512124444_7a35f64a2e019dc6d8622d3b65ed7e1a, https://doi.org/10.1016/0377-0427(87)90125-7

Schmucker, U. (1970). Anomalies of geomagnetic variations in the southwestern United States. *Bulletin of the Scripps Institution of Oceanography*, *13*, 33–53.

Sevastopulo, G. D., & Wyse Jackson, P. N. (2009). Carboniferous (Dinantian). In I. S. Holland, & C. H. Sanders (Eds.), *The Geology of Ireland*, (2nd ed.pp. 241–288). Edinburgh: Dunedin Academic Press.

SLR (2011). *Geothermal play fairway analysis*. Dublin: Sustainable energy authority of Ireland.

Smirnov, M. Y. (2003). Magnetotelluric data processing with a robust statistical procedure having a high breakdown point. *Geophysical Journal International*, *152*(1), 1–7. https://doi.org/10.1046/j.1365-246X.2003.01733.x

Somerville, I. D., & Strogen, P. (1992). Ramp sedimentation in the Dinantian limestones of the Shannon Trough, Co. Limerick, Ireland. *Sedimentary Geology*, *V*(79), 59–75. https://ac.els-cdn.com/003707389290004B/1-s2.0-003707389290004B-main.pdf?_tid=c9c41744-d67e-11e7-8ee4-00000aab0f6c&acdnat=1512122750_7f50cbd668edabe4a8bdb9bf3349953f

Somerville, I. D. (2008). Biostratigraphic zonation and correlation of Mississippian rocks in Western Europe: Some case studies in the late Viséan/Serpukhovian. *Geological Journal*, *43*(2–3), 209–240. https://doi.org/10.1002/gj.1097

Soyer, W., & Brasse, H. (2001). A magneto-variation array study in the Central Andes of N Chile and SW Bolivia. *Geophysical Research Letters*, *28*(15), 3023–3026. https://doi.org/10.1029/2000GL012095

Strogen, P., Somerville, I. D., Pickard, N. A. H., Jones, G. L. L., & Fleming, M. (1996). Controls on ramp, platform and basinal sedimentation in the Dinantian of the Dublin Basin and Shannon Trough, Ireland. *Geological Society, London, Special Publications*, *107*(1), 263–279. https://doi.org/10.1144/GSL.SP.1996.107.01.19

Tao, Z., & Clarens, A. (2013). Estimating the carbon sequestration capacity of Shale formations using methane production rates. *Environmental Science & Technology*, *47*(19), 11318–11325. https://doi.org/10.1021/es401221j

Teichmüller, H., Teichmüller, R., & Weber, R. (1979). Inkohlung Und Illit-Kristallinität. Vergleichende Untersuchungen Im Mesozoikum Und Paläozoikum von Westfalen. *Fortschritte in der Geologie von Rheinland und Westfalen*, *27*, 201–276.

Tietze, K., & Ritter, O. (2013). Three-dimensional magnetotelluric inversion in practice—The electrical conductivity structure of the San Andreas Fault in Central California. *Geophysical Journal International*, *195*(1), 130–147. https://doi.org/10.1093/gji/ggt234

Weise, H. (1962). Geomagnetische Tiefentellurik. *Pure and Applied Geophysics*, *52*, 83–103.

Wight, D. E., & Bostick, F. X. (1980). *Cascade decimation--A technique for real time estimation of power spectra* (pp. 626–629). Denver, Colorado, USA: IEEE.

Willmot Noller, N. M., Daly, J. S., & the IRETHERM team (2015). The contribution of radiogenic heat production studies to hot dry rock geothermal resource exploration in Ireland. Proceedings World Geothermal Congress, Melbourne, Australia

Worthington, R. P., & Walsh, J. J. (2011). Structure of lower carboniferous basins of NW Ireland, and its implications for structural inheritance and Cenozoic faulting. *Journal of Structural Geology*, *33*(8), 1285–1299. https://doi.org/10.1016/j.jsg.2011.05.001

References From the Supporting Information

Booker, J. R. (2014). The magnetotelluric phase tensor: A critical review. *Surveys in Geophysics*, *35*(1), 7–40. https://doi.org/10.1007/s10712-013-9234-2

Caldwell, T. G., Bibby, H. M., & Brown, C. (2004). The magnetotelluric phase tensor. *Geophysical Journal International*, *158*(2), 457–469. https://doi.org/10.1111/j.1365-246X.2004.02281.x

Jones, A. G. (2012). Distortion of magnetotelluric data: Its identification and removal. In A. D. Chave & A. G. Jones (Eds.), *The Magnetotelluric Method: Theory and Practice* (pp. 219–302). Cambridge, UK: Cambridge University Press.